

# Predictability of Arctic Annual Minimum Sea Ice Patterns

GARY GRUNSEICH

*Department of Atmospheric Sciences, and International Pacific Research Center,  
University of Hawai'i at Mānoa, Honolulu, Hawaii*

BIN WANG

*Department of Atmospheric Sciences, and International Pacific Research Center, University of Hawai'i at Mānoa,  
Honolulu, Hawaii, and Earth System Modeling Center, Nanjing University of Information Science  
and Technology, Nanjing, China*

(Manuscript received 29 January 2016, in final form 27 June 2016)

## ABSTRACT

Prediction of the arctic annual sea ice minimum extent and melting patterns draws interest from numerous industries and government agencies but has been an ongoing challenge for forecasters and climate scientists using statistical and dynamical models. Using the dominant independent modes of interannual sea ice concentration (SIC) variability during September–October, a new approach combining statistical analysis with physically derived links to natural climate variability sources is used to predict each mode and the total anomaly pattern. Sea ice patterns associated with each mode are predominantly shaped by the wind-driven advective convergence, forced by circulation anomalies associated with local and remote forms of naturally occurring climate variability. The impacts of the Arctic Oscillation, beginning from the preceding winter, control the leading mode of SIC variability during the annual minimum. In the three final months of the melting period, the broad impacts of the Indian and East Asian summer monsoons produce unique SIC impacts along the arctic periphery, displayed as the second and third modes, respectively. El Niño–Southern Oscillation (ENSO) largely shapes the fourth SIC mode patterns through influencing variability early in the melting period. Using physically meaningful and statistically significant predictors, physical–empirical (P–E) models are developed for each SIC mode. Some predictors directly account for the circulation patterns driving anomalous sea ice, while the monsoon-related predictors convey early season sources of monsoonal variability, which subsequently influences the Arctic. The combined SIC predictions of the P–E models exhibit great skill in matching the observed magnitude and temporal variability along the arctic margins during the annual minimum.

## 1. Introduction

Interannual variability accounts for a large percentage of the variance of summer arctic sea ice on time scales longer than the annual cycle and has been increasing in recent years, indicating year-to-year forecasts of the

annual minimum extent could become more challenging in the future (Vihma 2014). Arctic sea ice variability has been linked to midlatitude influences on weather and climate on many time scales by driving anomalous wave trains, changing storm tracks, and altering the jet stream, and thus accurate sea ice prediction could lead to improved climate forecasts (Cohen et al. 2014; Hopsch et al. 2012; Honda et al. 2009; Tang et al. 2013). Alternatively, recent and long-term fluctuations of arctic circulation, temperature, and sea ice have been driven by remote wave train patterns originating in the Pacific, which act on decadal and longer time scales (Wettstein and Deser 2014; Ding et al. 2014). Year-to-year prediction of the annual sea ice minimum extent using a variety of dynamical, statistical, and heuristic techniques from the arctic research community, solicited by the

---

School of Ocean and Earth Science and Technology Publication Number 9742, International Pacific Research Center Publication Number 1208, and Earth System Modeling Center Publication Number 118.

---

*Corresponding author address:* Bin Wang, International Pacific Research Center, University of Hawai'i at Mānoa, POST 401, 1680 East-West Rd., Honolulu, HI 96822.  
E-mail: wangbin@hawaii.edu

DOI: 10.1175/JCLI-D-16-0102.1

study of environmental arctic change (SEARCH) program (SEARCH 2015), has shown mixed results but ultimately exhibits difficulty in matching observations (Stroeve et al. 2014; Hawkins et al. 2016). The recent rise of human activities and interest in arctic resources from a number of industries has made accurate ice forecasts a significant priority (Eicken 2013). The ensemble of predictions analyzed by Stroeve et al. (2014) shows recent years where the September mean extent is matched well between ensemble models and observations while other years where the actual extent is outside the ensemble range or where the observations and ensemble means are close but the ensemble spread is large. The ensemble of predictions exhibits the greatest difficulty during extreme ice volume years.

The prediction errors, which use conditions in the preceding 2–4 months, suggest summer synoptic conditions, early spring sea ice conditions, and model methods could all contribute to forecasting difficulties. Therefore a combined approach accounting for the processes shaping early season ice conditions and prediction of summer arctic atmospheric patterns could aid in a more successful prediction. The long-term declining sea ice volume has resulted in larger expanses of thin ice, which are more sensitive to atmospheric variations in the summer (Holland et al. 2008; Stroeve et al. 2012). A recent rise in the ice drift speeds has been observed, confirming the thinning ice sheet is responding more strongly to the local wind forcing (Kwok et al. 2013; Vihma et al. 2012).

Sea ice concentration (SIC), or ice fractional area, in many models is predicted using the same governing equation developed by Thorndike et al. (1975). The fundamental equation predicts an ice thickness distribution function for each grid point dependent on sea ice thermodynamic melt, sea ice divergence, and a parameterized redistribution function representing mechanical ridging and opening processes. SIC is handled as a discrete variable that is measured by calculating the fractional area occupied by a set thickness range (Hunke and Lipscomb 2010).

Movement and divergence of sea ice is strongly driven by local winds and currents. Many studies have shown that the geostrophic wind is the predominant driver of sea ice motion at distances far (exceeding 400 km) enough from coastal effects (Thorndike and Colony 1982; Zhao and Liu 2007). When relating ice motion to low-level geostrophic winds, thick ice and the ice in close proximity to the coast generally move more slowly than thin ice and ice at greater distances from the coast (Kimura and Wakatsuchi 2000). Seasonally, summer sea ice motion has a higher multiplier, which describes the relation between the sea ice and geostrophic wind speeds, compared to other seasons (Thorndike and Colony

1982). Sea ice in the seasonal sea ice zone, the region from the permanent ice margin to the maximum sea ice extent boundary, accounts for the quickest ice motion in the Arctic owing to a lower internal ice stress compared to the central Arctic, which is specifically related to the ice thickness (Hibler 1979; Overland and Pease 1988). Thorndike et al. (1975) highlight the dominant processes shaping sea ice in the following equation:

$$\frac{\partial g}{\partial t} = -\nabla \cdot (vg) - \frac{\partial}{\partial h}(fg) + \psi, \quad (1)$$

where  $g$  is a probability distribution function representing ice thicknesses within a grid,  $v$  is ice velocity,  $f$  is the growth rate,  $h$  is ice thickness, and  $\psi$  is a thickness redistribution function. Sea ice deformation, determined by spatial gradients in the motion of sea ice, plays a large role in high frequency (<1 month) variability in sea ice thickness, while transport plays a larger role on interannual time scales (Lindsay et al. 2003; Thorndike et al. 1975; Watanabe and Hasumi 2005; Kauker et al. 2003). The relatively rapid motion of ice, especially in the seasonal sea ice zone, during the summer months makes the advective convergence term in the governing sea ice thickness equation [second term in Eq. (1)] the primary factor for investigating summer interannual variability. Thin ice is more likely to deform, making the arctic margins during the summer specifically prone to advective convergence effects (Vihma 2014).

On the annual cycle, thermodynamic melt [third term in Eq. (1)] has the greatest influence on ice thickness variability (Thorndike et al. 1975). Oceanic and atmospheric heat fluxes acting on the bottom and top of the ice sheet, working in combination with the thermal history of the ice, the current ice thickness, snow coverage, and brine content, act to influence the annual sea ice thickness. During winter, the thermodynamic growth rate of sea ice is nonlinear with ice thicker than 3 m generally exhibiting a growth rate roughly two orders of magnitude less than ice found in a newly refreezing region. The summer melt rate is weakly dependent on thickness as most of the mass changes occur on the ice sheet surface.

Previous work has separated leading modes of SIC variability but have retained the annual and decadal components or were too focused on a specific locale to make interannual variability in the summer easily distinguishable (Walsh 1980; Singarayer and Bamber 2003). Early attempts at sea ice area and edge prediction often relied heavily on the properties of sea ice such as ice volume, ice extent, and ice thickness in the months preceding the forecast period of interest (Chevallier and Salas-Méllia 2012; Guemas et al. 2016; Goessling et al.

2016). While this approach has produced favorable results, it relies heavily on accurate measurements of sea ice properties that can be difficult to collect with a widespread resolution. The goal of the present study is to identify the major modes of interannual SIC variability during the annual minimum, link them to natural forms of climate variability, and develop a prediction tool based on the leading modes. Emphasis is placed on the physical processes linking natural anomalous atmospheric circulations to anomalous sea ice patterns by focusing on the major driver of interannual SIC variability, transport. The data and methodology for determining the SIC modes and developing the prediction models are discussed in section 2. Section 3 shows a brief validation of current dynamical models, section 4 examines the natural sources of interannual SIC variability during September–October, and section 5 elaborates on the development of a new interannual SIC prediction model. The skill of the newly developed physical–empirical (P–E) sea ice model for interannual variability during the annual sea ice minimum extent is assessed in section 6. The final section summarizes our findings, highlights unresolved issues, and discusses possibilities for continued improvement.

## 2. Data and methods

Monthly bootstrap SIC from *Nimbus-7* Scanning Multichannel Microwave Radiometer (SMMR) and Defense Meteorological Satellite Program (DMSP) Special Sensor Microwave Imager–Special Sensor Microwave Imager/Sounder (SSM/I–SSMIS) version 2 is utilized for the 1979–2013 period (Comiso 2000). This SIC dataset has a 25-km resolution on a  $304 \times 448$  SSM/I polar stereographic grid. To remove the long-term nonlinear declining trend in the summer (September–October) SIC, the 3-yr running mean is subtracted out, acting like a weighted 6-yr filter to focus on interannual variability. For the end years, the 3-yr mean is the first or last 3-yr sequence. Empirical orthogonal function (EOF) analysis is conducted on the interannual SIC data averaged over September–October of each year since the period surrounding the annual minimum is highly dynamic and exhibits the greatest difficulty in prediction.

Reanalysis monthly sea ice thickness (SIT), ice motion vectors, advective convergence, and thermodynamic melt from the Pan-Arctic Ice Ocean Model and Assimilation System (PIOMAS; Zhang and Rothrock 2003) were used to understand sea ice variations prior to the annual melt and widespread breakup of arctic sea ice and determine the major processes [Eq. (1)] shaping sea ice variability (Thorndike et al. 1975). These data are available on a  $360 \times 120$  generalized curvilinear grid

covering latitudes north of  $45^\circ\text{N}$ . Monthly rainfall rate from the Climate Prediction Center Merged Analysis of Precipitation (CMAP; Xie and Arkin 1997) and Global Precipitation Climatology Project (GPCP) version 2.2 combined precipitation dataset (Adler et al. 2003) from 1979 to 2013 on a global  $2.5^\circ$  grid were averaged together by month following the methodology in Yim et al. (2014a). Monthly NCEP–DOE Reanalysis-2 geopotential height, sea level pressure (SLP), sea surface temperature (SST), and wind are used to discern the circulations that are associated with various teleconnection patterns. Using regressed 200-hPa fields of geopotential heights and winds, the wave activity flux is calculated to determine the energy propagation along the teleconnections, which is parallel to the group velocity of the quasi-stationary Rossby wave trains (Plumb 1985).

Although Stroeve et al. (2012) demonstrate the difficulties of various model types in representing interannual sea ice area variability during the annual minimum, we follow up using spatial SIC data, which allow for a better understanding of specific arctic regions where model shortcomings are greatest, rather than an areal extent. Determining the regions where the models are exhibiting difficulty could reveal the unique dynamics in different sections of the Arctic that are not being accurately represented. Using CMIP5 historical runs from 1979 to 2005, the best models representing the average sea ice area, long-term trend, time span of summer duration, and annual range of sea ice area (Zhou 2014) are selected for further analysis. These models include 1) CSIRO's Australian Community Climate and Earth-System Simulator (ACCESS 1.0), 2) NCAR's Community Earth System Model (CESM1 BGC), 3) Geophysical Fluid Dynamics Laboratory's Climate Model, version 3 (GFDL CM3), 4) Hadley Centre Global Environment Model version 2–Atmosphere and Ocean (HadGEM2-AO), 5) Hadley Centre Global Environment Model version 2–Carbon Cycle (HadGEM2-CC), and 6) Max Planck Institute Earth System Model, low resolution (MPI-ESM-LR). Similar to the observed SIC data, the long-term declining trend is removed by subtracting out the 3-yr running mean to focus on the interannual component.

### *P–E model development*

The goal of the P–E model is to independently predict the leading EOF modes that account for a large percentage of the overall variance, using physical relationships with key observed variables, and then perform hindcast experiments for verification (Wang et al. 2015a). Rather than searching for predictors in a variety of oceanic and atmospheric fields, we examine the persistence and tendency of SLP, SST, and 2-m air

temperature anomalies since these variables uniquely represent various climate forcings (Wang et al. 2015b). Lead-lag as well as simultaneous correlations between the leading modes and predictor variables are performed to empirically detect the most important patterns associated with each mode and how they relate to natural forms of interannual climate variability.

Potential predictors are selected based on the spatial average within the statistically significant and physically meaningful regions of interest similar to Lee et al. (2011). Using the lead-lag correlations between each SIC EOF mode in September–October and the persistence and tendency variables, boxes are drawn around key regions exhibiting both high correlations and physical meaning identified in previous work. Each potential predictor, specific to each mode, is standardized by its standard deviation and is loaded into a stepwise regression. This allows for the contribution of each predictor and major source variability to be determined by examining the coefficients in each term of the regression equation. The stepwise regression utilizes an  $F$  test to reject potential predictors that are insignificant at the 95% significance level, which when considered in the regression could act to increase/decrease the regressed variance. To determine the robustness of the selected predictors and ensure overfitting is minimized, a cross validation is performed by removing 3 years of data from each time step from 1979 to 2013 and predicting the central missing year using remaining years and the established predictors.

A validation of the physical–empirical method is performed by computing the variance of the combined EOF modes relative to the interannual observations of SIC or fractional signal variance. The fractional signal variance shows how much of the observed interannual variability is represented by the four leading EOF modes and portrays the upper limit of the P–E model as well as cross-validated P–E model capability. Additionally, correlations of the combined EOF modes and historical simulations of the P–E model and cross-validated P–E prediction model with the observed interannual component of SIC are computed. This reveals the potential predictability of this method in different locations and shows where the P–E models are performing best in the Arctic.

### 3. Assessment of interannual variability in historical model runs

Comparisons of the interannual component of the CMIP5 historical simulations of SIC with satellite-derived observations reveals the shortcomings of dynamical models to properly represent variability on the

year-to-year time scale. The ratio of the modeled interannual variance to the observed interannual variance (fractional signal variance) reveals that the models are largely underrepresenting the variability along the ice sheet margins and overestimating the variance by as much as 20 times in the less dynamic inner core of the ice sheet (Fig. 1). The Beaufort to eastern East Siberian Seas, Laptev Sea, Kara Sea, and North Atlantic Arctic are all regions where the year-to-year variance is consistently disproportionately small between all models.

Even with the long-term decline removed out of the September–October modeled SIC, very few regions in the Arctic exhibit moderate correlations with observations (Fig. 2). In all six models, the central core region of the arctic ice sheet exhibits poor correlations, which is concerning since this is a region with little interannual variability to begin with. The MPI-ESM-LR performs best along the arctic periphery showing high correlations in the East Siberian and coastal Laptev Seas. The inability to properly match the observed interannual magnitude and signal of the SIC variations from 1979 to 2005 indicates the processes governing year-to-year variability need to be better represented in order for dynamical models to be used as an accurate forecasting tool.

### 4. The leading September–October interannual SIC predictable modes

Interannual SIC variability is mainly confined to the seasonal sea ice zone, defined in this study as the region from the inner 10% seasonal SIC change between the annual maximum and minimum depicting the permanent ice margin to the 0% SIC contour (Fig. 3). The combined explained variance of the first four EOF modes of observed interannual SIC variability in September–October account for 59.9% of the overall variance throughout the Arctic (Fig. 4). The leading mode, accounting for 25.3% of the variance, represents a zonally uniform pattern throughout the arctic seasonal sea ice zone that contrasts the Fram Strait and Greenland Sea region (Fig. 4a). Regressions of the EOF 1 mode with lower- (Figs. 5a,b) and upper-tropospheric (Figs. 6a,b) features during different periods leading up and through to the late summer reveal this mode is strongly linked to winter North Atlantic Oscillation (NAO)/Arctic Oscillation (AO)-type patterns as shown by the anomalous SLP dipole over the North Atlantic and Europe (Fig. 5a). In the early summer, the EOF 1 mode is strongly related to the opposing AO phase exhibited in the preceding winter as shown by the contrasting AO SLP pattern in June–August (Fig. 5b). This is consistent with earlier work (Rigor et al. 2002; Rigor and Wallace 2004) showing the high-phase winter AO (WAO; negative SLP



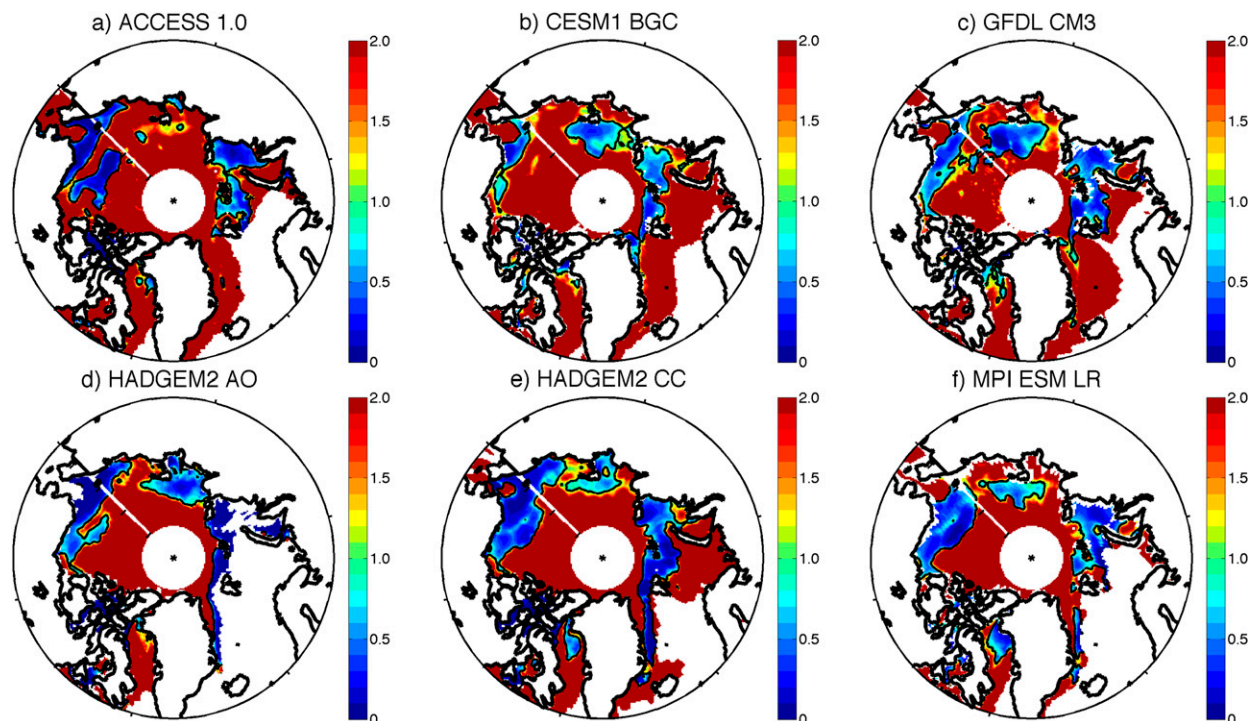


FIG. 1. Fractional signal variance of the top six CMIP5 model SIC historical runs to the overall observed interannual SIC variance from 1979 to 2005 during September–October.

anomalies centered over the Arctic) acts to dynamically thin sea ice from the Eurasian Arctic to Beaufort Sea through divergence of sea ice away from the coasts. In the following summer, a low-phase AO (anomalously higher arctic SLP) further acts to reduce arctic sea ice coverage through southward transport to the North Atlantic where the sea ice eventually melts. The regression analysis of the EOF 1 mode in this case during the two time periods reflects the processes that were previously identified and will be referred to as the AO mode.

The EOF 2 mode, accounting for 14.2% of the interannual SIC variability in September–October, represents a tripole-like pattern with the Greenland Sea, Beaufort Sea, and Chukchi Sea regions contrasting the Eurasian arctic region (Fig. 4b). Regressions of the second SIC mode in January–May (Figs. 5c and 6c) reveal no easily discernible link of this mode with global climate features. However, the June–August regressions with the EOF 2 mode show an eastward-propagating circumglobal barotropic Rossby wave train coupled with the subtropical jet (Ding and Wang 2005; Ding et al. 2011), which links Indian summer monsoon (ISM) rainfall with arctic circulation after a North Atlantic/European bifurcation (Figs. 5d and 6d). The ISM teleconnection creates an arctic barotropic dipole structure in which a cyclonic circulation is centered

over the Barents and Kara Seas and an anticyclonic circulation extends over the East Siberian, Chukchi, and Beaufort Seas. These circulations are responsible for driving sea ice out of the Laptev Sea and into the Fram Strait leading to negative and positive SIC anomalies, respectively. The positive SIC anomalies in the Beaufort and Chukchi Seas are created by wind-driven advective convergence of sea ice along the western flank of the positive SLP circulation. Because of the strong connection with ISM rainfall and the circumglobal teleconnection, this second interannual SIC mode will appropriately be named the ISM mode.

Accounting for 11% of the interannual SIC variance, the EOF 3 mode represents variability in the western East Siberian Sea, Laptev Sea, and Beaufort Sea contrasting the North Atlantic Arctic, Kara Sea, and areas north of the Chukchi Sea (Fig. 4c). Regression analysis of the EOF 3 in January–May shows a marginal SLP and wave train that represents an ENSO-type pattern (Figs. 5e and 6e), while the June–August period exhibits a meridional barotropic wave train extending out of the East Asian summer monsoon (EASM) domain into the Arctic (Figs. 5f and 6f). These results show the dipole-like behavior between western North Pacific summer monsoon (WNPSM) and EASM rainfall and strong meridional links to arctic circulation previously

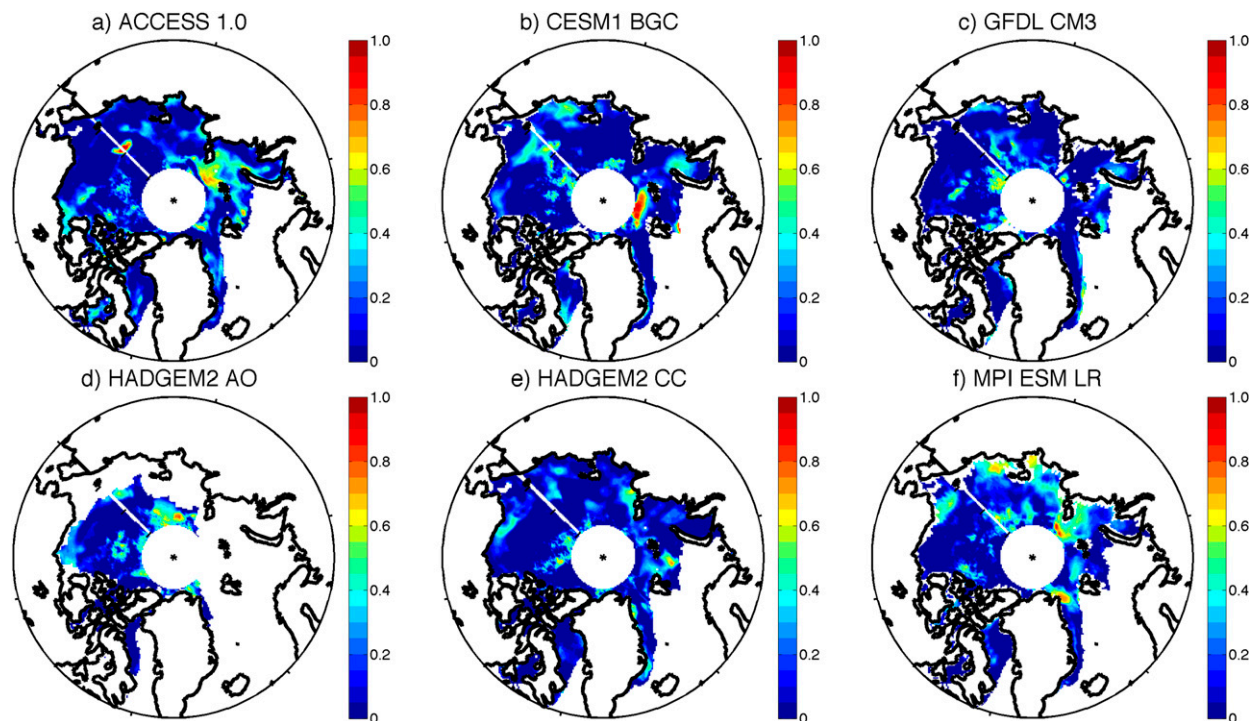


FIG. 2. As in Fig. 1, but for correlation coefficients.

discussed in Nitta (1987), Lau and Weng (2000), and Lau et al. (2004). The anomalous anticyclonic circulation centered over the Arctic builds up sea ice in the Beaufort Sea while also transporting it out of the Chukchi Sea and into the western East Siberian and Laptev Seas. Additionally, interannual EASM monsoon variability is often preceded by ENSO conditions during the winter months (Wang et al. 2000) consistent with the regression maps for the EOF 3 mode. While the EASM-related SIC variability peaks in the early summer (June–August), the impacts are still prevalent, albeit weaker and slightly modified, as the third mode in September–October. The consistency of this third mode with earlier work earns it the aptly named EASM mode.

The fourth EOF mode, explaining 9.4% of the variance, represents variability in the North Atlantic Arctic contrasting the inner Beaufort to East Siberian Seas (Fig. 4d). Of all the leading modes, it begins to account for higher magnitudes of interannual SIC variability in the inner core of the Arctic. Regressions of the EOF 4 mode with the January–May period show this mode is strongly related to ENSO (Figs. 5g and 6g), which gradually decays by June–August (Figs. 5h and 6h). The anomalous regressed fields during the early spring period show contrasting precipitation patterns between the eastern and western equatorial Pacific Ocean as well

as positive and negative upper-level geopotential height anomalies corresponding to the anomalous latent heating. Anomalous Rossby wave trains extend out of the northern tropical Pacific Ocean and influence arctic circulation north of Alaska and Canada similar to Ding et al. (2014). In light of the strong links with ENSO, the EOF mode will be referred to as ENSO mode.

### 5. Predictor selection for the leading interannual SIC modes

Based on early literature and the analysis from the previous section, key regions in which observed variables exhibit meaningful links to natural forms of climate variability are chosen as potential predictors. The potential predictors are the spatial average in the statistically significant (at 90% to maximize the spatial area) region within each chosen box. Each selected location has a physical meaning and specific time period based on previous work, although the time period of the predictor selection maximized the lead to September–October SIC.

A total of 34 potential predictors for each of the modes were established. Potential predictors are disregarded if there is no discernible physical link between the highly correlated areas and natural climate variability that

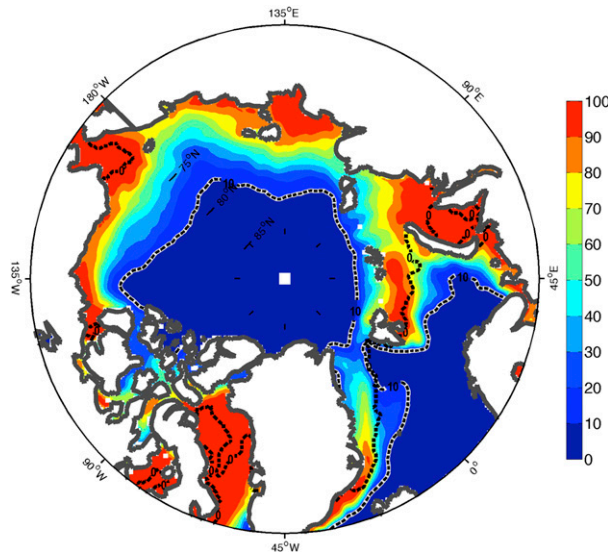


FIG. 3. SIC difference between March and September averaged sea ice concentration. Black and white contour shows the 10% SIC difference between the annual maximum and minimum while the dashed contour shows the average location of the 0% SIC margin during September. The area between the inner 10% seasonal SIC change and the average 0% SIC September contour is defined as the seasonal sea ice zone.

shapes sea ice. The potential predictors were loaded into a stepwise regression where an  $F$  test rejected potential predictors that are too correlated with others and retained the ones with that best capture the predictands. The final predictors that were considered were rigorously tested to make sure they 1) induce an appropriate sea ice response via wind-driven forcing and if remotely forced 2) induce a wave train pattern that influences the arctic low-level circulation in a way that explains the appropriate sea ice EOF pattern. The combination of these methods ensures the predictors have physical and statistical meaning.

#### a. The AO mode predictors

Correlations with the persistence and tendency of a number of climatic variables leading the annual sea ice minimum extent were used to empirically determine the best predictors for each mode but also the physical link between the variable and SIC mode. In the case of the AO mode, correlation maps reveal a strong link (correlation coefficients reaching over  $r = 0.5$ ) to January–April SLP anomalies in the North Atlantic extending into Europe (Fig. 7a). This dipole pattern in the anomalous pressure field between the southeastern North Atlantic and northern Europe is consistent with a WAO-type pattern highlighted in Deser (2000). The areal averages within regions with significant correlations can be objectively selected and used as a predictor for the SIC AO mode (Table 1).

The AO mode also produces a unique correlation pattern during the June–August period in the SLP anomaly (SLPA) field with correlations reaching over  $r = 0.6$  (Fig. 7b). A meridional dipole between the Northern Hemisphere midlatitudes and high latitudes is consistent with a summer AO (SAO)-type pattern. The sign change in the correlations between late winter and early summer is consistent with previously discussed results indicating this SIC mode is related to the combined effects of a reciprocating AO occurring during the melting season. The regions of significant correlations with this mode are used as a predictor for the SIC AO mode since they are robust and are linked to verified forms of climate variability (Table 1).

To understand the connections of each predictor to the September–October SIC variability associated with each mode, regressions are performed using the selected predictors and various climate variables. The WAO predictor regression with SLP, sea ice motion, and SIT in January–April shows sea ice transport from the Asian Arctic toward the Canadian archipelago, closely following the low-level geostrophic wind associated with the anomalous negative SLP pattern over the North Atlantic (Fig. 8a). The importance of the AO forced wind field on shaping sea ice has been highlighted on a number of different time scales (Deser and Teng 2008; Ogi and Yamazaki 2010). Throughout the northern Siberian Arctic, SIT is reduced up to 0.3 m, with most of the anomalies concentrated in the East Siberian Sea, while the Canadian region shows an increase exceeding 0.3 m in thickness due to wind-driven advective convergence of sea ice [second term in Eq. (1)]. Kauker et al. (2003) demonstrate that the AO-related SIT anomalies created during the winter months can translate to concentration anomalies during the following summer and hence the SIT anomalies, particularly in the Siberian Arctic, could contribute to reduce concentration in the summer. The winter SIT anomalies along the Canadian Islands and Greenland do not translate to summer SIC anomalies since annual concentrations in this area do not decline below 100%. The SAO predictor exhibits an anomalous high SLP circulation centered over the Arctic in June–August (Fig. 8b). The sea ice transport follows the clockwise motion of the 1000-hPa wind field and the general transport of ice out of the Arctic during a negative summer AO pattern (Kauker et al. 2003; Watanabe and Hasumi 2005). The positioning of the anomalous high pressure favors the accumulation of arctic sea ice in the North Atlantic before it melts as it continues its southward trajectory. The SAO predictor accounts for the general decline of SIC zonally along the arctic margins and rise in SIC in the North Atlantic as ice is transported into this region.



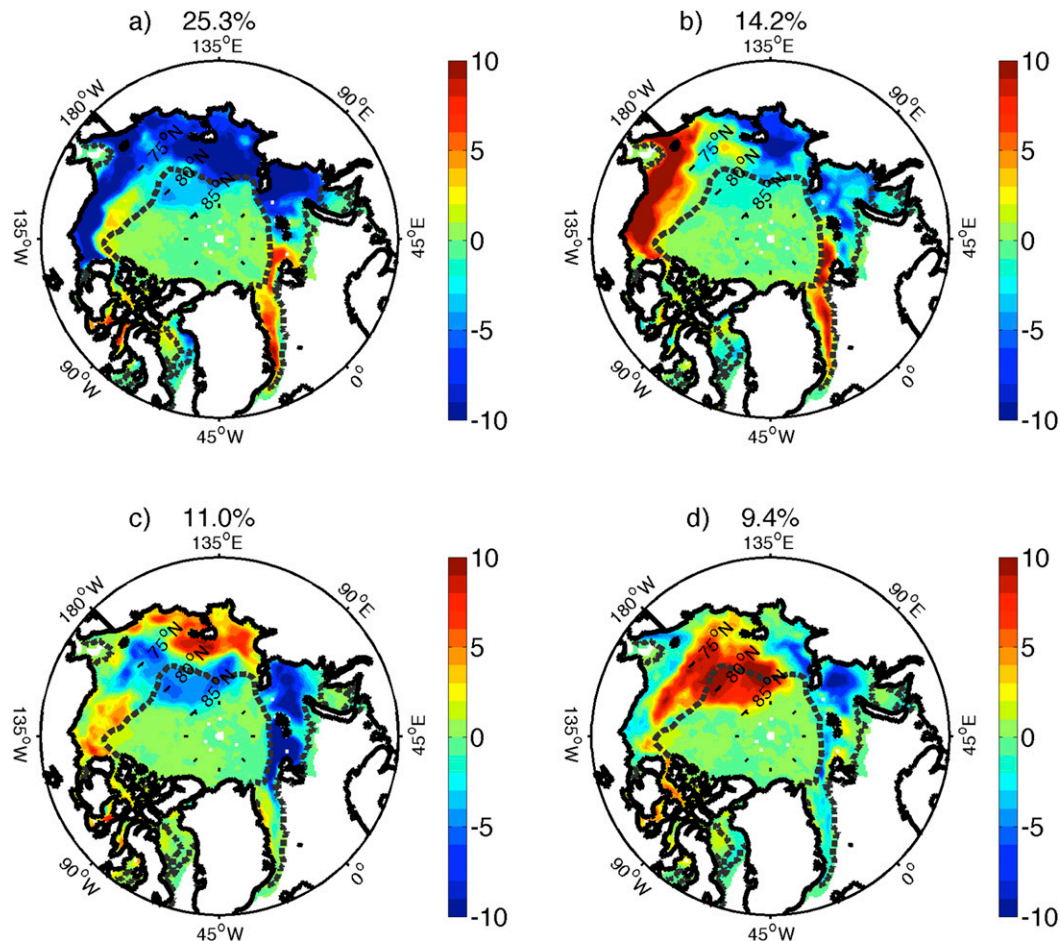


FIG. 4. Leading four EOF modes in September–October interannual SIC observations from 1979 to 2013. Each mode has been standardized and regressed to give units of anomalous sea ice concentration. Dashed contour shows the seasonal sea ice zone.

The SAO predictor shows a much stronger correlation to the SIC AO mode than the WAO predictor, indicating that the conditions in immediate period leading up to the annual sea ice minimum are more important in this case than the late winter or early spring (Table 2). The coefficients in the regression equation demonstrate this further by heavily weighting the SAO predictor over the WAO. However, the low correlation between the two predictors for the AO mode indicated both yield key information to successfully represent this September–October mode. The P–E model using the WAO and SAO predictors exhibits a temporal correlation of  $r = 0.76$  with the AO mode indicating a close relationship.

#### b. The ISM mode predictors

The ISM (EOF 2) SIC mode in September–October exhibited significant negative correlations exceeding  $r = -0.6$  with the anomalous SLP tendency between

March and May over East Asia (Fig. 7c). This springtime pattern is consistent with Wang et al. (2015b), who showed other than ENSO-related predictors, enhanced ISM rainfall co-occurs with a declining SLP tendency centered over Lake Baikal in the spring. While directly using the ISM rainfall as a predictor for the EOF 2 mode would provide the highest forecast skill, the forecast lead time if taken in July–August is not ideal if possible earlier predictors can be established. The Lake Baikal predictor, representing the Asian pressure tendency (APT), which we have aptly named the APT predictor, is selected using correlations with the SIC EOF 2 mode but is more related to influences on the ISM, which drives arctic sea ice variability (Table 1). Regressions of the APT predictor with June–August anomalous 200-hPa geopotential height, wave activity flux, and rain rate show, although not fully, the eastward-propagating circumglobal Rossby wave train associated with the

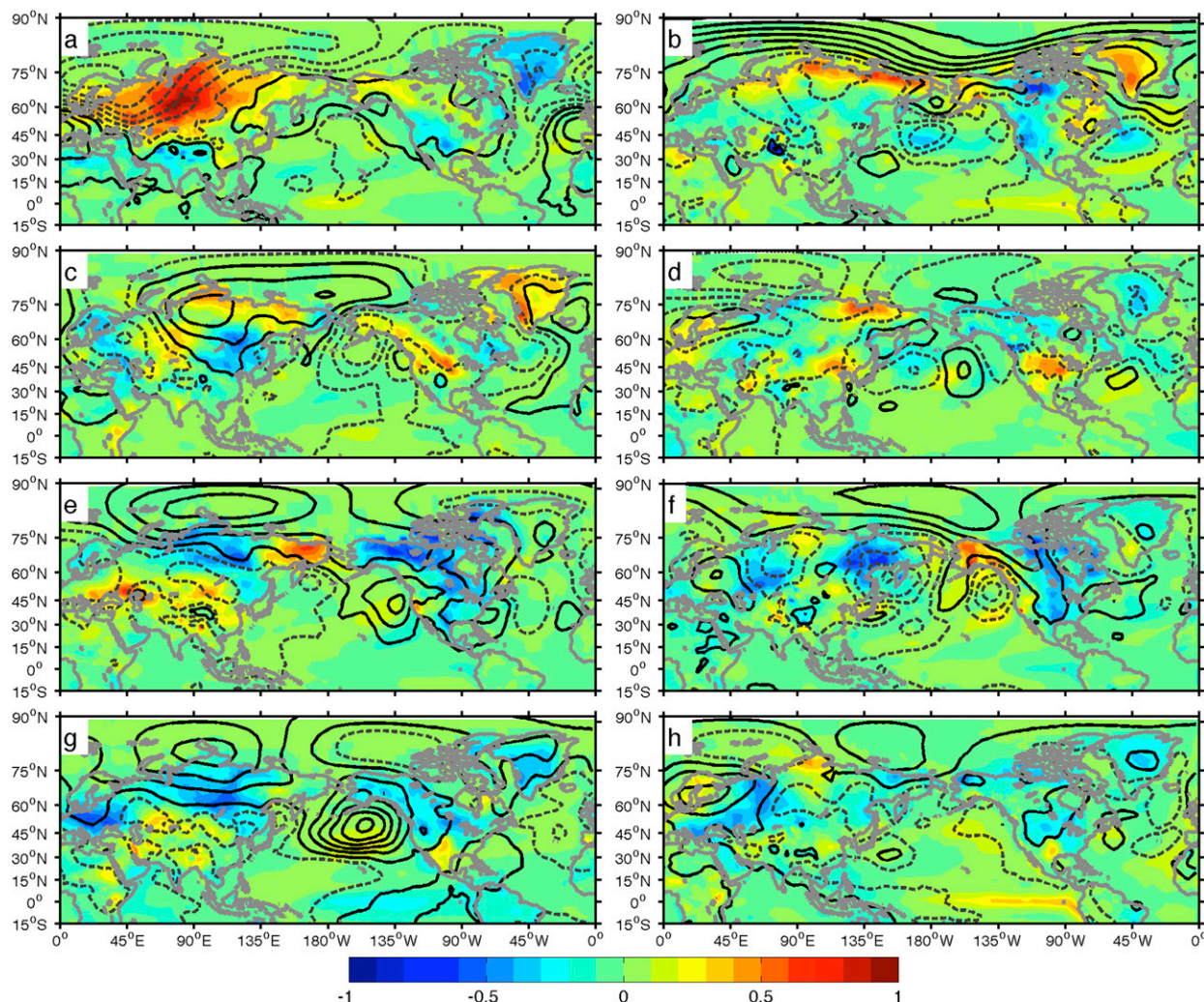


FIG. 5. Anomalous global SST (shading; °C), 2-m air temperature (shading; °C), and SLP (contoured every 0.3 hPa with solid being positive values) during (left) January–May (left) and (right) June–August regressed with (a),(b) EOF 1, (c),(d) EOF 2, (e),(f) EOF 3, and (g),(h) EOF 4.

enhanced ISM rainfall (Fig. 9a). The wave train originates northwest of India and follows the subtropical jet at roughly 45°N into the North Atlantic, closely following the pattern outlined in Ding and Wang (2005). We show this pattern continues northward and produces a barotropic dipole circulation pattern over the Arctic after a bifurcation over Europe. The APT predictor, reflecting ISM variability, also captures the anomalous SIC pattern in which negative SIC anomalies develop in the Laptev Seas while positive anomalies grow in the Beaufort and Chukchi Seas from wind-driven ice advective convergence (Fig. 9c). Sea ice is transported out of the Laptev Sea, as observed by the ice motion vectors, by the pressure gradient between the anomalous anticyclonic and cyclonic circulations that develop over the Arctic. Along

the southern flank of the high pressure anomaly, sea ice is transported into the Beaufort and Chukchi Seas by the geostrophic wind field.

The second selected predictor is related to an anomalous dipole SST tendency pattern between the western and eastern Indian Ocean during Jan and May (Fig. 7d and Table 1). This predictor reflects the conditions associated with an emerging Indian Ocean dipole (IOD) pattern where anomalously low SST, the result to wind-driven upwelling by southeasterlies along the Indonesian coast, are accompanied by reduced precipitation during the summer and early fall (Saji et al. 1999; Webster et al. 1999). In the western Indian Ocean, anomalous westward transport along the equator raises SST and enhances precipitation in the following months. The IOD enhances monsoonal flow and convection by



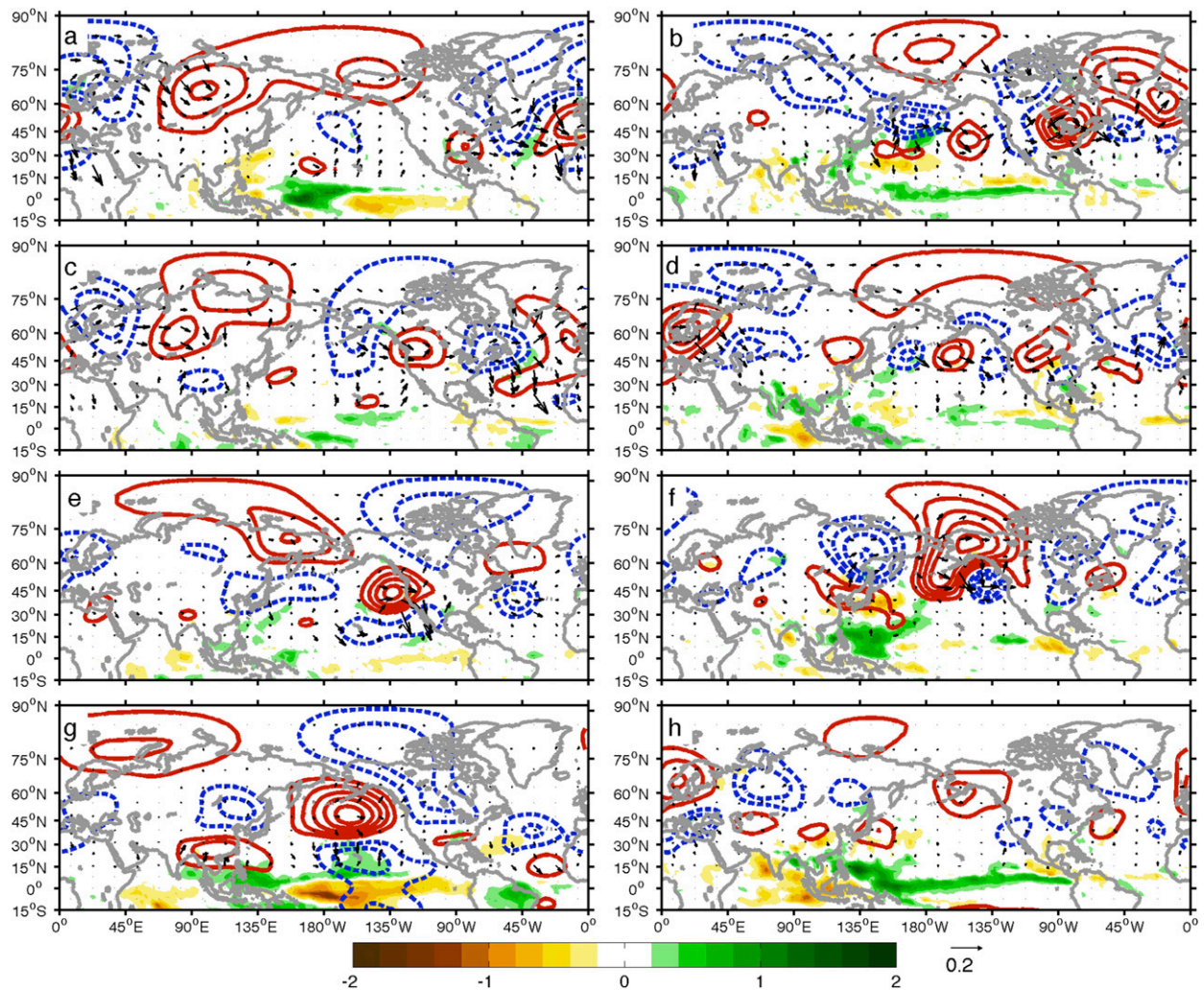


FIG. 6. Anomalous rain rate (shading;  $\text{mm day}^{-1}$ ), wave activity flux (vectors;  $\text{m}^2 \text{s}^{-2}$ ), and 200-hPa geopotential height (contoured every 4 m with red being positive values) during (left) January–May and (right) June–Aug regressed with (a),(b) EOF 1, (c),(d) EOF 2, (e),(f) EOF 3, and (g),(h) EOF 4.

strengthening the northward branch of the Rossby wave response to the eastern Indian Ocean cooling (Wang and Xie 1996; Wang et al. 2003, 2004; Xiang et al. 2011). This influence of the IOD on ISM rainfall explains the high correlations between this predictor and the second SIC EOF 2 mode when taking into account the ISM–Arctic link. Similar to the APT predictor, the IOD predictor reflects most of the circumglobal teleconnection pattern associated with the ISM, the arctic barotropic dipole circulation pattern, and enhanced ISM rainfall but also the equatorial Indian Ocean rainfall pattern typical of a positive IOD event (Fig. 9b). Eastern equatorial Indian Ocean precipitation anomalies show a widespread decline, while western tropical Indian Ocean precipitation shows a subtle rise, both of which are modulated by the anomalous zonally varying SST.

In the Arctic, the anomalous circulation and sea ice patterns associated with the IOD predictor are consistent with the APT and ISM patterns exhibiting sea ice transport out of the Laptev Sea resulting in negative SIC anomalies and sea ice convergence into the Fram Strait and Beaufort and Chukchi Seas during June–August (Fig. 9d).

The APT and IOD predictors have comparable moderate correlations with the SIC EOF 2 mode (Table 2). The low correlation between the two ISM mode predictors indicates they uniquely contribute to ISM rainfall variability and make them ideal variables to load into the stepwise regression model. Although the P–E model for the ISM mode is a little more heavily weighted on the APT predictor, they are the most analogous regression coefficients out of all the



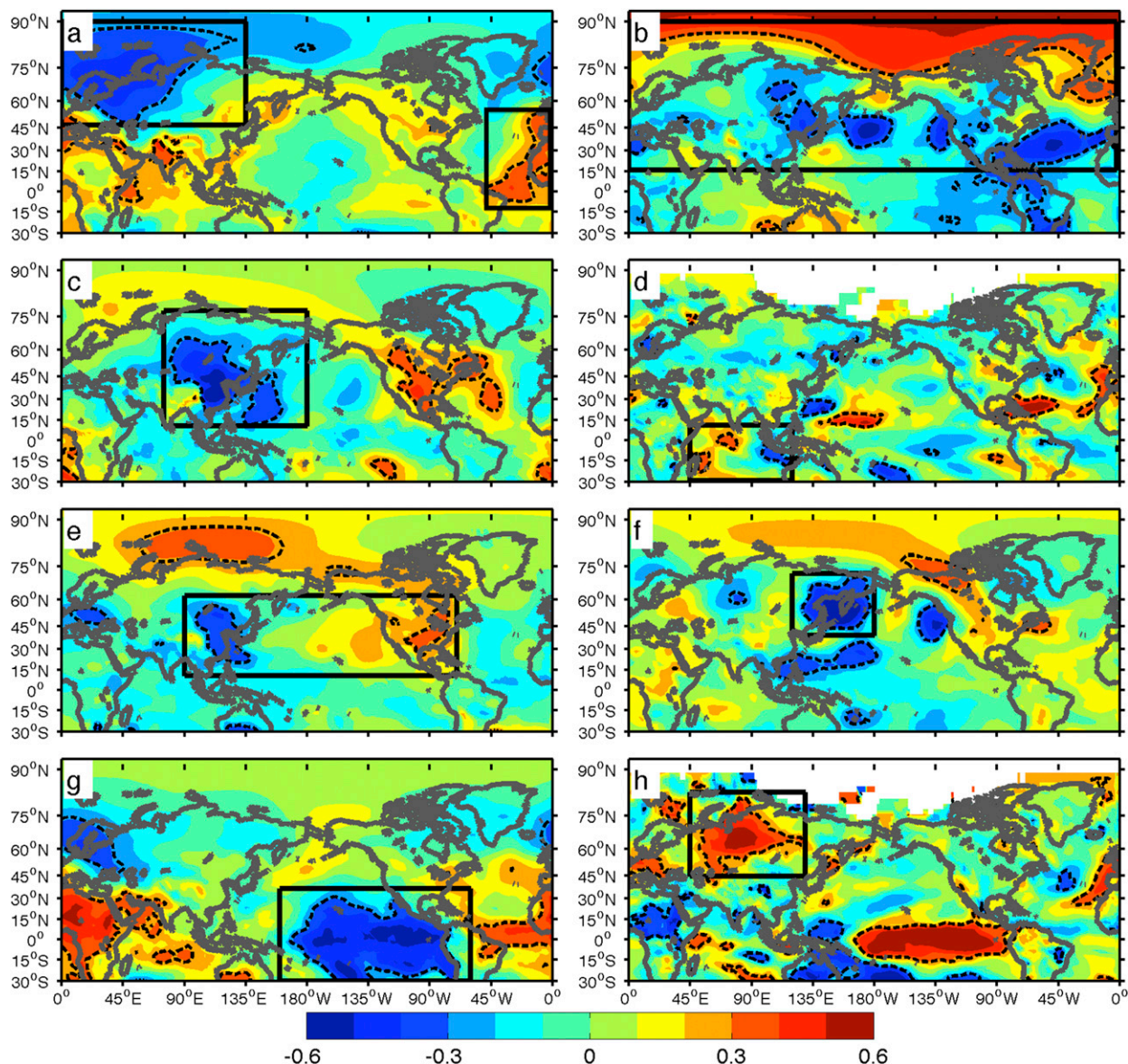


FIG. 7. Predictors selected based on correlation maps of (a) EOF 1 and January–April mean SLPA, (b) EOF 1 and June–August SLPA, (c) EOF 2 and May–minus–March SLPA, (d) May–minus–January SST anomaly (SSTA), (e) EOF 3 and January–March mean SLPA, (f) EOF 3 and June–August mean SLPA, (g) EOF 4 and April–minus–January SLPA, and (h) EOF 4 and May–minus–January 2-m temperature anomaly (2MTEMPA). Spatial averages are taken in the statistically significant regions (dashed contours show the 90% significance level) within each box. When positive and negative correlations occur within the same box, each is standardized and the difference is taken.

developed P–E models. Using the APT and IOD predictors in this P–E model produces a high temporal correlation of  $r = 0.74$  with the ISM mode.

### c. The EASM mode predictors

The interannual SIC EASM (EOF 3) mode exhibits a unique continental pressure dipole (CPD) between East Asia and North America in the January–March mean SLP anomaly correlation field (Fig. 7e). We used the

difference between these two statistically significant regions to create the CPD predictor, which resembles ENSO-like conditions. Regressions of this predictor with climate variables in January–April show negative geopotential height and precipitation anomalies in the tropical eastern North Pacific while the western North Pacific displays positive precipitation and geopotential height anomalies (Fig. 10a). Poleward-propagating wave trains, with the east Pacific wave train being

TABLE 1. Definitions of each predictor for the leading interannual SIC modes. DSLP, DSST, and D2MT denote the tendency of each variable.

Mode	Name	Meaning	Definition
AO mode	WAO	Jan–Apr averaged North Atlantic SLP dipole	SLP ( $45^{\circ}$ – $87.5^{\circ}$ N, $0^{\circ}$ – $135^{\circ}$ E)–SLP ( $15^{\circ}$ S– $55^{\circ}$ N, $310^{\circ}$ – $357.5^{\circ}$ E)
	SAO	Jun–Aug averaged N. hemisphere SLP dipole	SLP ( $15^{\circ}$ – $87.5^{\circ}$ N, $0^{\circ}$ – $357.5^{\circ}$ E) difference
ISM mode	APT	May–minus–Mar East Asian SLP	DSLP ( $10^{\circ}$ – $75^{\circ}$ N, $75^{\circ}$ – $180^{\circ}$ E)
	IOD	May–minus–Jan Indian Ocean SST east–west dipole	DSST ( $30^{\circ}$ S– $10^{\circ}$ N, $45^{\circ}$ – $120^{\circ}$ E) difference
EASM mode	CPD	Jan–Mar averaged Asia–North America SLP dipole	SLP ( $10^{\circ}$ – $60^{\circ}$ N, $90^{\circ}$ – $290^{\circ}$ E) difference
	MTT	Jun–Aug averaged northeast Asia SLP	SLP ( $37.5^{\circ}$ – $70^{\circ}$ N, $120^{\circ}$ – $180^{\circ}$ E)
ENSO mode	EPP	Apr–minus–Jan eastern equatorial Pacific SLP	DSLP ( $30^{\circ}$ S– $35^{\circ}$ N, $160^{\circ}$ – $300^{\circ}$ E)
	IAO	May–minus–Jan northwest Asia 2-m temp	D2MT ( $43^{\circ}$ – $80^{\circ}$ N, $45^{\circ}$ – $130^{\circ}$ E)

stronger, position a barotropic anticyclonic circulation over the northern Pacific extending into the Arctic, which helps to weakly drive sea ice into the western East Siberian and Laptev Seas (Fig. 10c). While in this case the arctic forcing using this predictor is not strong, ENSO conditions often precede anomalous WNPSM and EASM rainfall intensity. Decaying El Niño conditions often lead to weakened WNPSM rainfall and an enhanced EASM by strengthening the spring–summer western North Pacific anticyclone, which helps to bolster the mean trades along the eastern flank and cool SSTs through evaporative and entrainment cooling (Wang et al. 2000, 2001). Along the western edge of the anomalous anticyclone, the mean northeasterly monsoonal winds are weakened allowing for a rise in SST

centered in the South China Sea and enhanced convection. During a La Niña, conditions and processes typically reverse. While not strongly related to arctic anomalies in this case, the CPD predictor can be considered an early indicator of the dipole behavior in interannual WNPSM and EASM rainfall variability, which has been linked to the Arctic using the second predictor for the EASM SIC mode.

The second predictor for the EASM mode uses June–August mean SLP anomalies in northeast Asia and captures the meridional tripole teleconnection (MTT) associated with the EASM (Fig. 7f). The MTT predictor we have developed captures the typical contrasting behavior between WNPSM and EASM rainfall as well as the poleward propagation of the barotropic

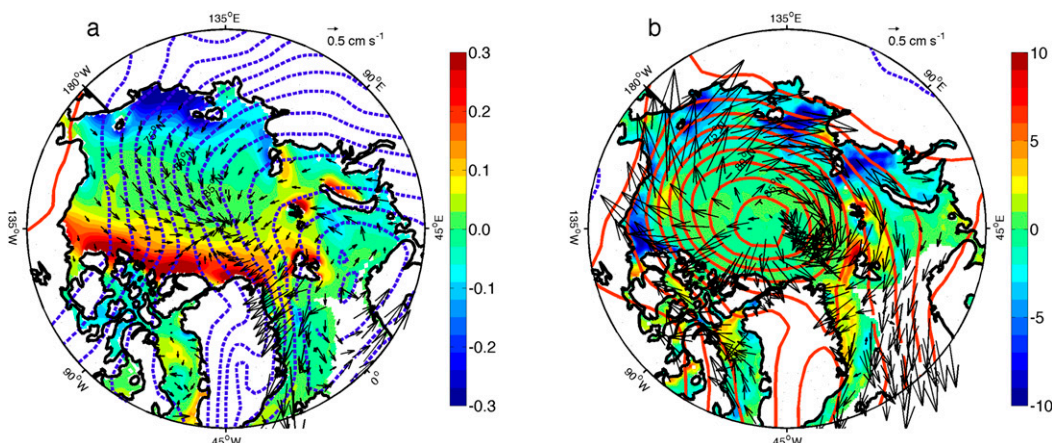


FIG. 8. (a) WAO index regressed with January–April averaged SIT (shading; meters), sea ice motion (vectors;  $\text{cm s}^{-1}$ ), and SLP anomalies (contoured every 0.3 hPa). (b) SAO index regressed with May–August averaged SIC (shading; %), sea ice motion (vectors;  $\text{cm s}^{-1}$ ), and SLP anomalies (contoured every 0.3 hPa).

TABLE 2. P–E model predictor correlation coefficients.

AO mode (EOF 1) predictand correlation coefficients and regression equation			
	AO mode	WAO	SAO
AO mode	1.00	0.48	0.68
WAO		1.00	0.20
SAO			1.00
AO mode = 0.3544 WAO + 0.6078 SAO			
ISM mode (EOF 2) predictand correlation coefficients and regression equation			
	ISM mode	APT	IOD
ISM mode	1.00	0.63	0.59
APT		1.00	0.35
IOD			1.00
ISM mode = −0.4830 APT + 0.4238 IOD			
EASM mode (EOF 3) predictand correlation coefficients and regression equation			
	EASM mode	CPD	MTT
EASM mode	1.00	0.52	0.62
CPD		1.00	0.29
MTT			1.00
EASM mode = 0.3731 CPD + −0.5153 MTT			
ENSO mode (EOF 4) predictand correlation coefficients and regression equation			
	ENSO mode	EPP	IAO
ENSO mode	1.00	0.60	0.53
EPP		1.00	0.13
IAO			1.00
ENSO mode = −0.5443 EPP + 0.4295 IAO			

Rossby wave train following the East Asian coast to the Arctic that is excited by the anomalous EASM heating (Fig. 10b; Nitta 1987; Lau and Weng 2000; Wang et al. 2001; Lau et al. 2004). The meridional EASM propagation centers an anticyclonic circulation over the Arctic with sea ice motion closely following the clockwise geostrophic wind field along the arctic margins (Fig. 10d). Wind-driven advective convergence, the dominant process shaping the SIC anomalies, helps to build up SIC anomalies in the Beaufort Sea region and contribute to a SIC reduction in the North Atlantic Arctic as ice is transported into the core of the Arctic in this region. The westward transport of sea ice helps to reduce SIC in the Chukchi Sea while strengthening SIC in the western East Siberian Sea, where sea ice builds up against the New Siberian Islands.

Correlations between the EASM mode and corresponding predictors show the MTT predictor is more closely related to the EOF 3 mode than the CPD predictor (Table 2), which is further verified by the stepwise regression placing a heavier weight on the MTT predictor. The low correlation between the MTT and CPD predictors makes them ideal variables for the P–E model and also suggests that although the EASM and

ENSO are strongly linked, the EASM variability and arctic influences can occur independently. The P–E model developed for the EASM mode exhibits a temporal correlation of  $r = 0.72$  with the third EOF.

#### d. The ENSO mode predictors

The fourth interannual SIC EOF mode, the ENSO mode, exhibits the largest and most widespread correlations with the SLP tendency between January and April (Fig. 7g). The strongest significant negative correlations are in the equatorial Pacific, which we spatially averaged to form the equatorial Pacific pressure (EPP) predictor. Regressions with rain rate show this predictor is strongly affiliated with anomalously dry conditions along the eastern equatorial Pacific contrasting the wetter conditions found in the western North Pacific (Fig. 11a). A strong Rossby wave response develops in response to the anomalous heating in which positive and negative geopotential height anomalies develop poleward of the wet and dry conditions, respectively. The characteristics of the precipitation and wave train patterns closely resemble the conditions found during a decaying ENSO mode during the spring months. A strong anticyclonic barotropic circulation develops over the northern Pacific Ocean and helps to transport sea ice by the low-level geostrophic wind from the East Siberian and Chukchi Seas into the Beaufort Sea as observed from the thickening SIT anomalies in January–April (Fig. 11c). As the season progresses, the anticyclonic circulation drifts to the northeast, shifting the wind-driven ice transport away from the Chukchi Sea and into the inner Arctic Ocean. While the EOF 4 mode exhibits high correlations with the SST tendency in the equatorial Pacific during the spring, which is strongly indicative of an ENSO-type pattern, this region is strongly connected to the EPP predictor and would be rejected in the stepwise regression model (Fig. 7h).

A region of significantly positive correlations in northwest Asia of January to May 2-m air temperature tendencies is selected as the second predictor for the EOF 4 mode. This predictor represents interseasonal AO (IAO) variability as the positive SLP anomaly migrates north-northeast during the spring and summer allowing for warming in northern Asia as cold air advection ends (Fig. 11b). Unlike the EOF 1 mode, which is related to an AO phase change during the spring, this predictor is related to a persistent AO phase from winter to summer and captures typical northward seasonal presentation of the AO SLP pattern. The anomalous high pressure during the spring months transports sea ice away from the Canadian and North Atlantic Arctic through the low-level



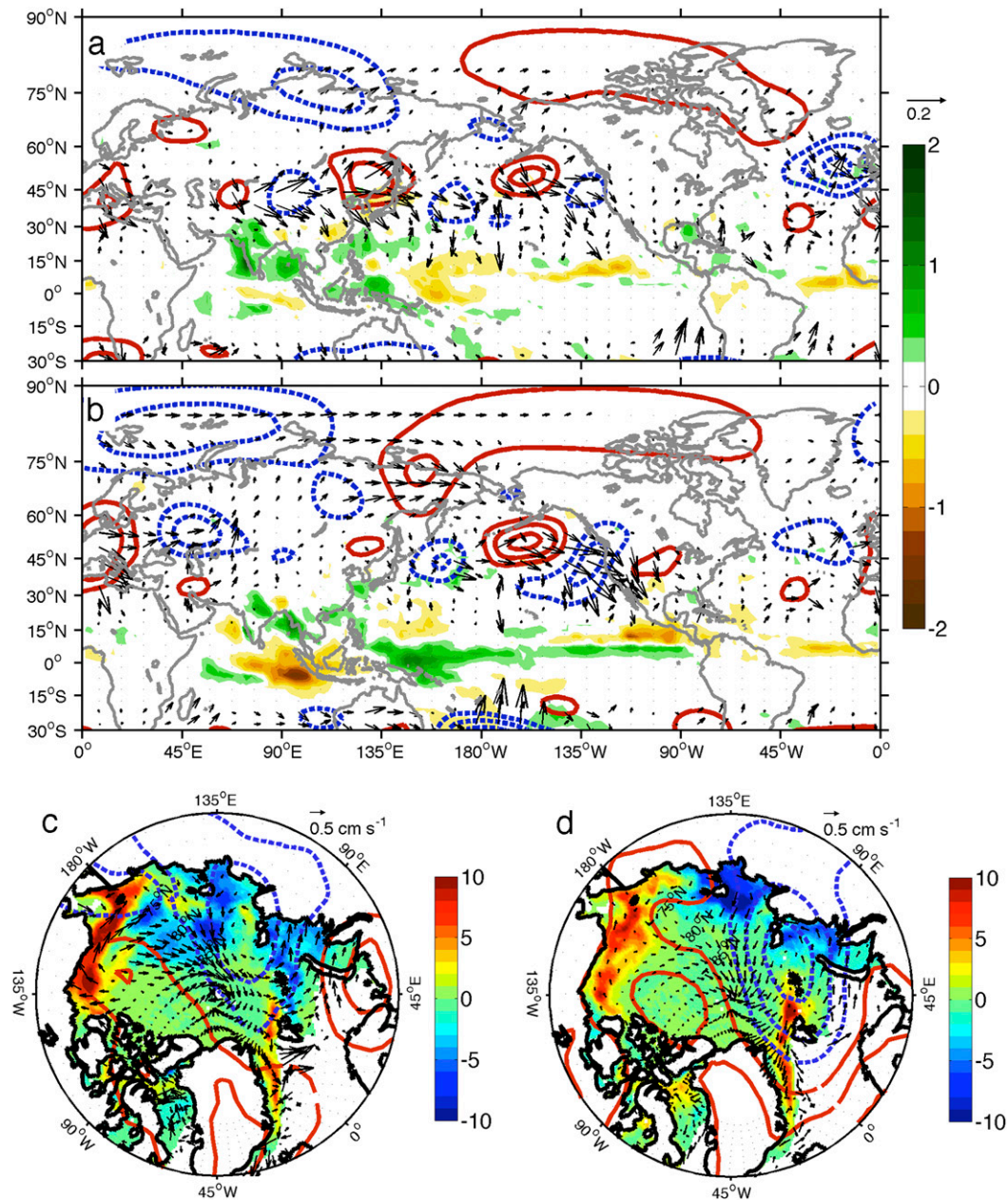


FIG. 9. June–August averaged rain rate (shading; mm day<sup>-1</sup>), wave activity flux (vectors; m<sup>2</sup> s<sup>-2</sup>), and 200-hPa geopotential height anomalies (contoured every 4 m with red being positive values) regressed with the (a) APT index and (b) IOD index. SIC (shading; %), sea ice motion (vectors; cm s<sup>-1</sup>), and SLP anomalies (contoured every 0.3 hPa) regressed with the (c) APT index and (d) IOD index.

geostrophic wind creating negative SIT anomalies. The anomalous high pressure is responsible for advective convergence of sea ice into the western East Siberian and Laptev Seas as the low-level circulation seasonally shifts from the North Atlantic to the North Pole (Fig. 11d).

The EPP predictor shares a stronger correlation ( $r = 0.6$ ) with the EOF 4 mode than the IAO predictor,

reaffirming this interannual SIC is strongly related to decaying spring ENSO conditions (Table 2). The EPP and IAO predictors exhibit an extremely low correlation with one another indicating they were ideal variables to be factored into the stepwise regression model. The P–E model for the ENSO mode places a stronger weight on the EPP predictor highlighting the importance of ENSO and remote forcings on arctic variability. The P–E model



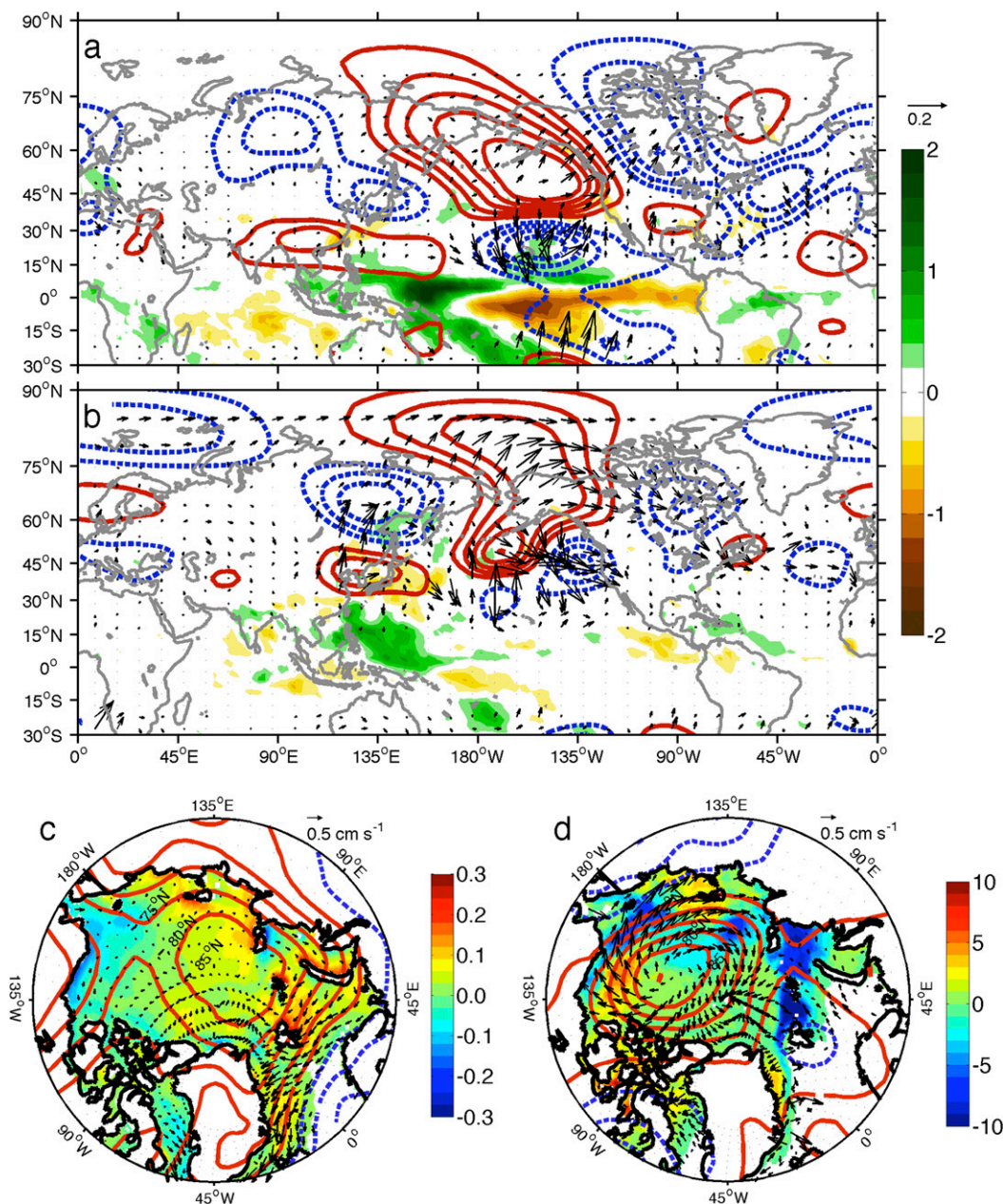


FIG. 10. January–April averaged rain rate (shading;  $\text{mm day}^{-1}$ ), wave activity flux (vectors;  $\text{m}^2 \text{s}^{-2}$ ), and 200-hPa geopotential height anomalies (contoured every 4 m with red being positive values) regressed with the (a) CPD index. June–August averaged rain rate (shading;  $\text{mm day}^{-1}$ ), wave activity flux (vectors;  $\text{m}^2 \text{s}^{-2}$ ), and 200-hPa geopotential height anomalies (contoured every 4 m with red being positive values) regressed with the (b) MTT index. SIT (shading; m), sea ice motion (vectors;  $\text{cm s}^{-1}$ ), and SLP anomalies (contoured every 0.3 hPa) regressed with the (c) CPD index. SIC (shading; %), sea ice motion (vectors;  $\text{cm s}^{-1}$ ), and SLP anomalies (contoured every 0.3-hPa) regressed with the (d) MTT index.

using the EPP and IAO predictors exhibits a temporal correlation of  $r = 0.76$  with the ENSO mode.

## 6. P–E model validation

To determine the total possible predictability of interannual SIC variability in September–October, the

first four EOF modes are combined and correlated with the observed interannual SIC data. The P–E model consists of the eight predictors (Table 1) and four stepwise regression equations (Table 2) that make use of the predictors. The prediction for each year is made by inputting the predictor values for the year of interest into

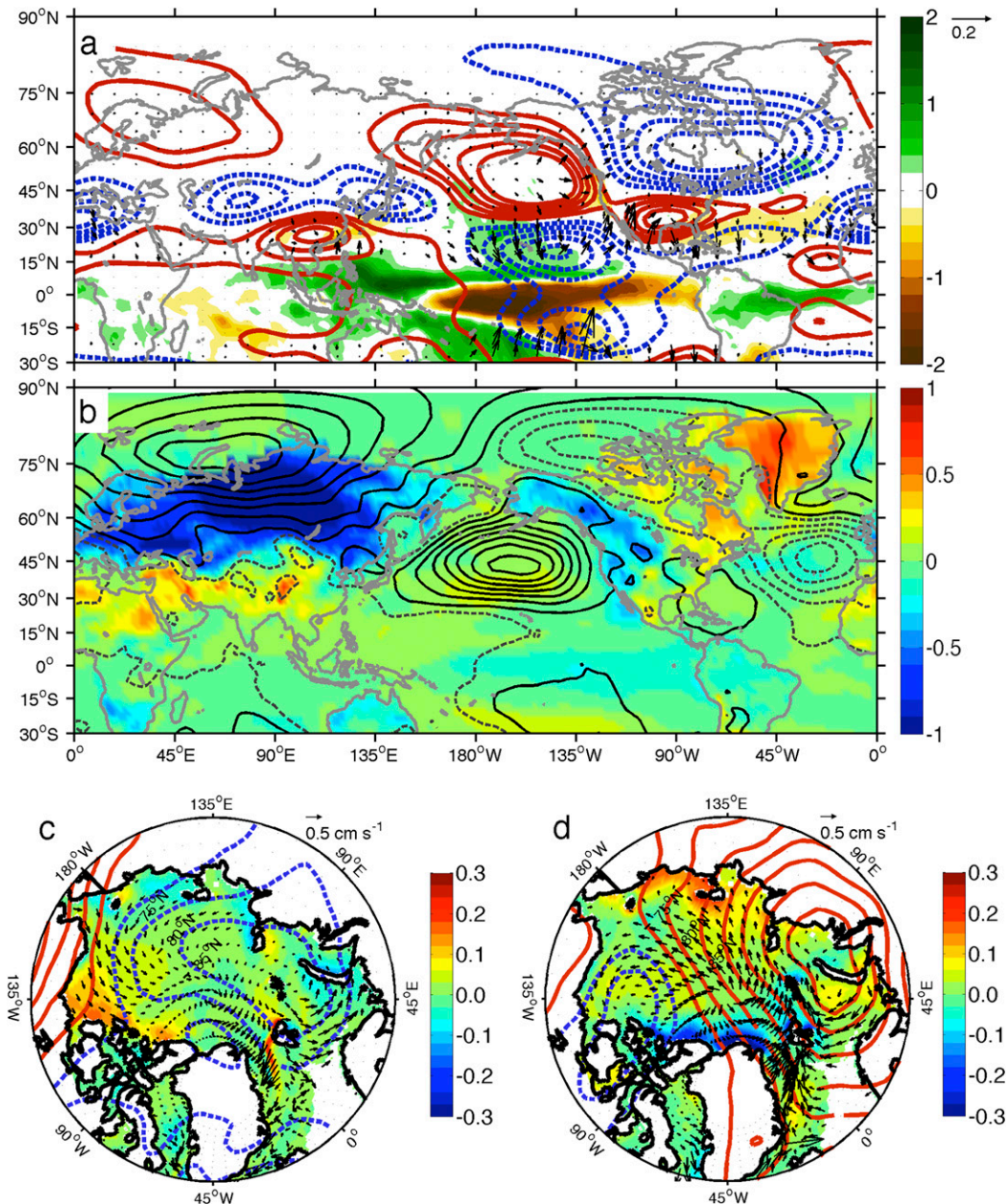


FIG. 11. January–April averaged rain rate (shading;  $\text{mm day}^{-1}$ ), wave activity flux (vectors;  $\text{m}^2 \text{s}^{-2}$ ), and 200-hPa geopotential height anomalies (contoured every 4 m with red being positive values) regressed with the (a) EPP index. January–April 2-m air temperature over land (shading;  $^{\circ}\text{C}$ ), SST (shading;  $^{\circ}\text{C}$ ), and SLP anomalies (contoured every 0.3-hPa with black being positive values) regressed with the (b) IAO index. SIT (shading; m), sea ice motion (vectors;  $\text{cm s}^{-1}$ ), and SLP anomalies (contoured every 0.3 hPa) regressed with the (c) EPP index and (d) IAO index.

the respective equations and computing a value for each mode. The spatial pattern for each mode is multiplied by its specific value from the model, acting to scale the respective patterns based on the climate phenomena from earlier in the year. The scaled spatial patterns for each mode are added to create that summer's prediction for

the anomalous sea ice patterns during September–October. Throughout the arctic margins, the first four EOF modes exhibit correlations of  $r = 0.8$  and higher, suggesting that these four modes account for a substantial portion of the total arctic variability along the periphery (Fig. 12a). Except for the eastern East



Siberian Sea, the fractional signal variance accounted for by the first four EOF modes in many regions of the arctic periphery is well over 80% (Fig. 12b). These modes do not account for variability in the inner core of the Arctic, Baffin Bay, or within the Canadian islands since they exhibit either 100% SIC and therefore no interannual variability or coastal influences obstruct the circulation influences on sea ice.

The variability of the combined four P–E models exhibits correlations throughout the arctic margins well over  $r = 0.5$  with the highest correlations in the Laptev, Kara, and western East Siberian Seas (Fig. 12c) and also accounts for widespread regions of over 50% of the interannual variance throughout the Arctic with the exceptions of the inner core and Baffin Bay (Fig. 12d). This holds true, to a lesser extent, for the cross-validated P–E models as well, indicating the interannual variability along the arctic margins in September–October is well represented by the established predictors (Figs. 12e,f). Within the seasonal sea ice zone the areal-averaged skill of the combined four leading EOF modes is  $r = 0.63$ , while the P–E models and cross-validated P–E models are  $r = 0.49$  and  $r = 0.44$ , respectively. The percentage of the total seasonal sea ice zone area ( $5.11 \times 10^6 \text{ km}^2$ ) that exhibits skills over  $r = 0.5$  for the combined four leading EOF modes is 87.6% ( $4.47 \times 10^6 \text{ km}^2$ ), while the P–E models and cross-validated P–E models are 72.7% ( $3.72 \times 10^6 \text{ km}^2$ ) and 57.3% ( $2.93 \times 10^6 \text{ km}^2$ ), respectively. The favorable spatial patterns in the correlation and fractional signal variance fields for the P–E model indicates the magnitude and temporal variability of the modeled SIC closely matches interannual SIC observations. Although variability in the inner core is not well represented in the P–E models and EOF modes, it represents little of the interannual variance. Sea ice coverage along the arctic periphery will have the largest impact on improving annual projections of minimum sea ice extent, and thus these four modes provide the greatest impact for advancement.

## 7. Discussion and concluding remarks

### a. Discussion

The motivation behind this work is to develop a practical forecasting tool for anomalous interannual SIC variability during the annual arctic minimum using a technique that has proven successful for prediction of other challenging meteorological phenomena. Even while initializing in June–August, current dynamical and statistical models have difficulty predicting sea ice extent and replicating the historical sea ice patterns during the annual arctic minimum. The newly developed P–E

model (Table 2) focuses on the leading modes of natural variability that drive sea ice during the lead-up to the annual minimum. Some of the predictors permit a long-lead prediction since winter variability can alter SIT anomalies, which persist into the summer and present as concentration anomalies as the sea ice thins and melts. While other P–E model predictors do not offer a long lead since they rely on climate variability in June–August, this time period corresponds to the initialization period for other model types. With these two P–E model predictor types in mind, the mechanisms and key points are further elaborated.

### 1) LONG-LEAD PREDICTORS

The seasonal progression of the AO and ENSO sea ice modes indicate that conditions and sea ice patterns created early in the year, when both forms of variability typically peak, carry through and manifest as summer SIC patterns. This evidence was first discussed on an interannual scale by Kauker et al. (2003), who found the first May–October mode from 1978–2001 is related to AO conditions shaping SIT anomalies in the leading winter. Typical SIT anomalies can persist for between 6 and 20 months with the duration and spatial scales being influenced by the initial thickness, season of formation, and transport (Blanchard-Wrigglesworth and Bitz 2014).

To get a better perspective of the progression and persistence of SIT into the summer as well as justify selection of early season predictors, we performed a month-by-month EOF analysis from January to August on interannual SIT. The annual progression of the leading SIT modes from winter to late summer is established by correlating the SIT modes from each month with those in the immediate preceding month since the order, pattern, and percent variance explained of leading interannual SIT modes vary month to month (Fig. 13). Besides matching corresponding modes, the monthly lagged correlations also show the periods when major changes in the SIT mode occur by exhibiting lower correlations and also periods of little change in the mode with high correlations.

The leading mode in the majority of the monthly periods corresponds to a SIT dipole between the Siberian Arctic contrasting the Canadian and North Atlantic Arctic (Fig. 14). The SIT anomalies develop from January to April, peak in magnitude and extent in May–June, and continue to persist until the annual sea ice minimum. The atmospheric and sea ice patterns closely match the WAO predictor for the AO mode (Fig. 8a), which contributes to the leading SIC interannual mode in September–October. The monthly lag correlations show this winter AO mode exhibits its lowest correlation

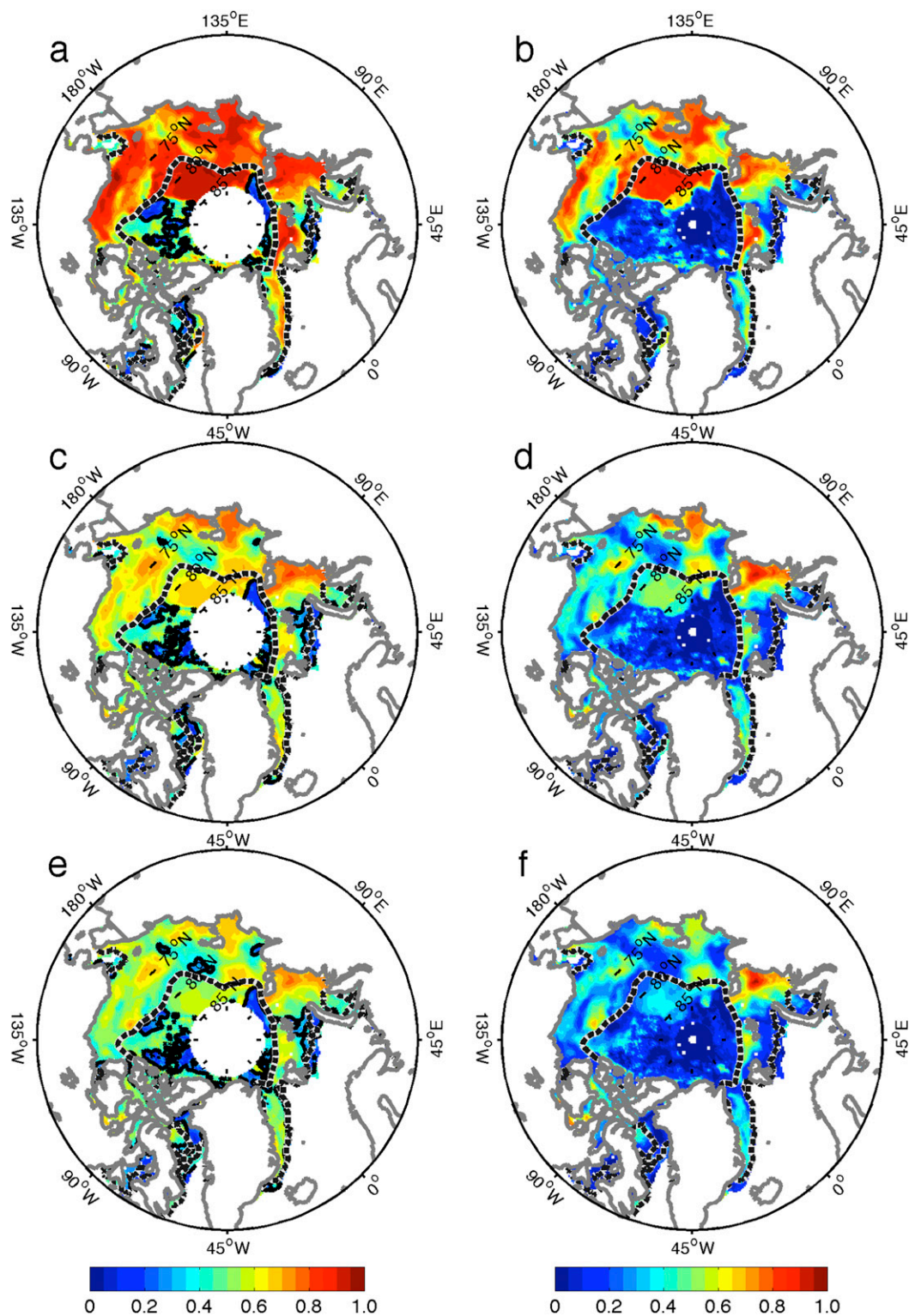


FIG. 12. (left) Correlation coefficients and (right) fractional signal variance of the combined (a),(b) leading four interannual SIC EOF modes, (c),(d) P-E models, and (e),(f) cross-validated P-E models with the observed interannual SIC from 1979 to 2013 during September–October. Solid contour represents the 95% significance level for the correlations while dashed line is the seasonal sea ice zone.

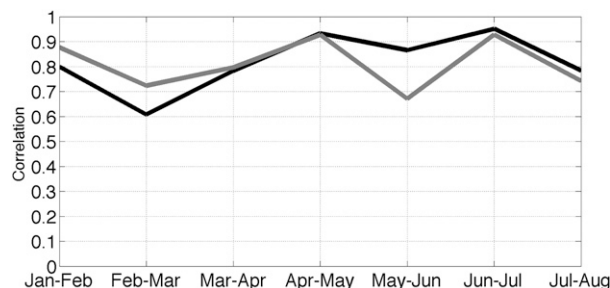


FIG. 13. Correlations between the typical first (black) and second (gray) interannual SIT modes in each month with the corresponding modes in the immediate preceding month. The correlations are used to match and create the monthly progressions of each mode since the order, pattern, and percent variance explained of the leading modes change from winter to late summer.

between February and March, indicating the most substantial change in the sea ice associated with this mode occurs during this time (Fig. 13). Anomalous low pressure builds into the North Atlantic Arctic during late winter and helps to create more consistent and widespread SIT anomalies in March than what was apparent in February (Fig. 14). After March, the monthly lag correlations rise showing the impacts of this mode consistently persist well into the summer months.

The typical second SIT month-by-month mode corresponds to the development of a summer-AO-type pattern closely resembling the SAO predictor (Fig. 8b). The summer AO mode in this case exhibits the lowest monthly lag correlation between May and June, which indicates major SIT changes occur during this time period (Fig. 13). Starting in June, high SLP anomalies build into the central Arctic and strengthen negative SIT anomalies along the arctic margins through transport of ice into the North Atlantic (Fig. 15). As the high strengthens throughout the summer, positive SIT anomalies become focused in the Fram Strait region through enhanced advective convergence along the east coast of Greenland. This SIT mode reinforces the combined impact of alternating AO phases between the winter and early summer months with the winter AO negative anomalies throughout the Siberian Arctic corresponding to locations of possible enhancement by the conditions of an opposing summer AO phase. The combined impacts of the winter and summer AO SIT modes account for 34.8%–42.7% of the total interannual variance depending upon the month of interest (Table 3) and are a valuable resource for improving sea ice coverage forecasting throughout the summer.

## 2) SHORT-LEAD PREDICTORS

While many of the predictors account for natural climate variability well in advance of the annual minimum

extent, there are two predictors that are taken in the period immediately preceding the annual minimum. The summer AO predictor for the AO mode is taken in June–August, capturing the meridional SLP dipole in the Northern Hemisphere and is opposite phase to the late winter AO conditions. The dynamics are consistent with previous studies and indicate that opposing AO phases between the winter and summer seasons have supportive influences on SIT and SIC and help to create the September–October EOF 1 pattern. This AO transition in May is a strong signal associated with the SIC EOF 1 mode and more work needs to be done to address the abrupt AO phase change. If the physical process behind this change can be explained, perhaps a predictor earlier in the season can be established.

The second EASM mode predictor (MTT) is also taken in June–August and directly accounts for the northward teleconnection forced by anomalous EASM rainfall. Establishing meaningful predictors for the EASM mode was difficult because of the CPD predictor link to ENSO. Many of the possible predictors investigated for this mode were overwhelmingly linked to ENSO conditions and highly correlated to the CPD predictor. The stepwise regression consistently rejected many of the early season predictors because of the high correlations with one another but consistently indicated the CPD predictor was most skillful. Since EASM mode accounts for 11% of the total interannual variance in September–October, the majority of interannual variability can still be predicted prior to the EASM peak and modified as the EASM progresses.

## b. Concluding remarks

About 60% of the total variance of observed interannual SIC variability throughout the entire Arctic in September–October, the annual minimum extent season, can be accounted for by the first four EOF modes. Local variability driven by the AO shapes the first leading mode while remote tropical variability forced by the ISM, EASM, and ENSO, respectively, shape the second, third, and fourth mode of sea ice coverage patterns by the end of the melt season. The inclusion of these higher-order modes, although representing consecutively smaller percentages of the overall variance, does improve the skill of the P–E model (Figs. 16a–c). While many of the P–E model predictors for each mode directly capture the features shaping the sea ice in the seasons prior to the annual minimum, the ISM and EASM predictors uniquely capture features influencing monsoonal variability, which impacts arctic climate during the summer months. The combined SIC anomalies predicted by the P–E models for the leading four EOF modes can realistically reproduce the historical



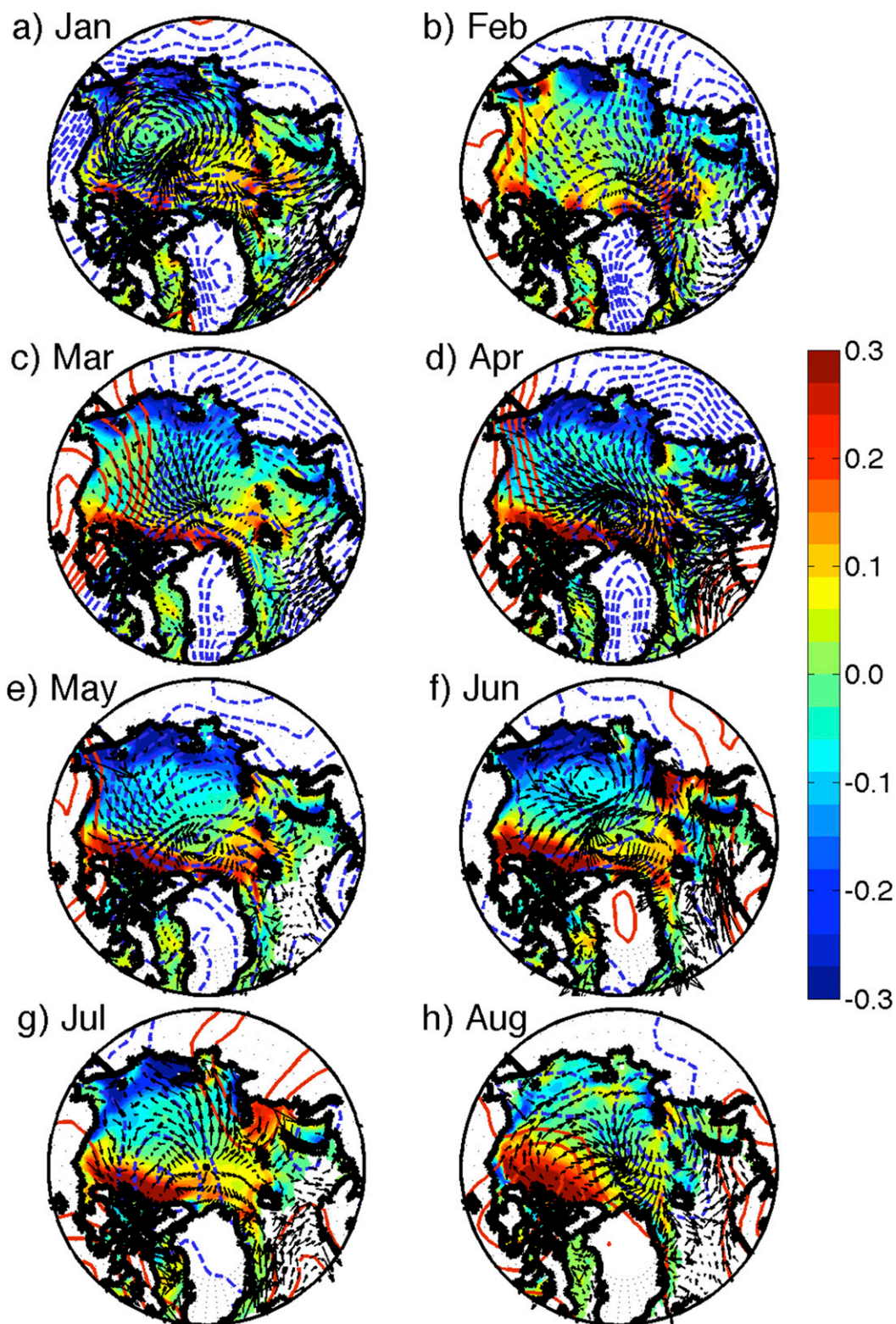


FIG. 14. The WAO SIT mode for each month regressed with SIT (shading; m), sea ice motion (vectors;  $\text{cm s}^{-1}$ ), and SLP anomalies (contoured every 0.3 hPa).

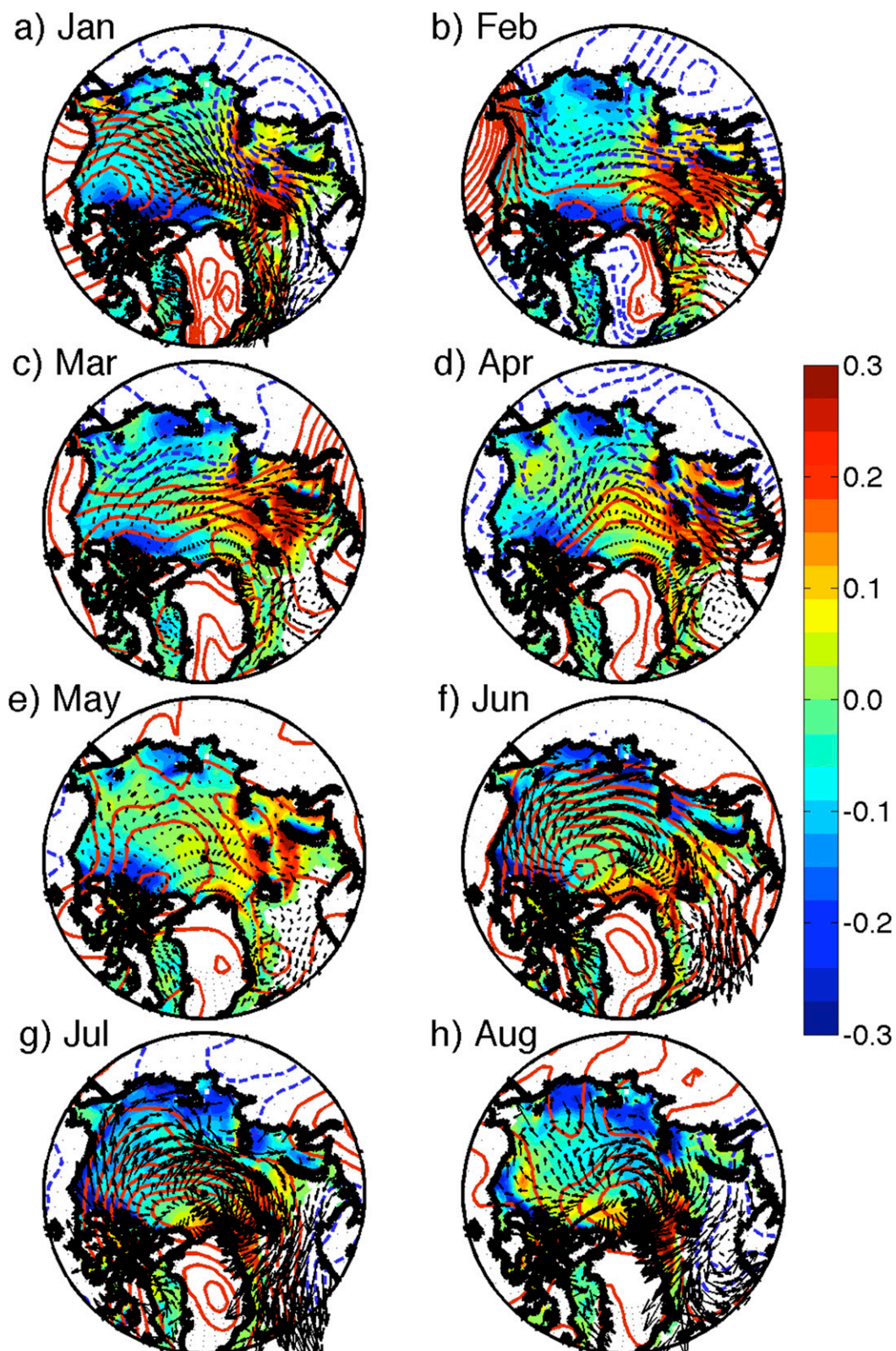


FIG. 15. As in Fig. 14, but for the SAO SIT mode.



TABLE 3. Percent variance explained by the leading SIT EOF modes for each month.

	Jan	Feb	Mar	Apr	May	Jun	Jul	Aug
WAO mode	14.55	15.71	19.25	24.87	25.75	25.71	18.02	17.89
SAO mode	23.54	19.50	15.49	14.64	13.58	17.01	21.05	20.76

interannual variability in satellite-derived SIC observations. Although two P–E model predictors rely on conditions immediately preceding the annual minimum sea ice extent, their inclusion does not substantially raise the skill of the overall modeled sea ice concentration patterns (Fig. 16d). Although this indicates meaningful predictions of the anomalous SIC pattern can be made using climate variability predictors prior to June, these

short-lead predictors are necessary to completely understand the sea ice links with climate variability.

Historical CMIP5 comparisons with observations reveal the shortcomings in correctly modeling the magnitude of interannual SIC variability during the annual minimum as well as matching the year-to-year signal throughout the Arctic. The difficulty exhibited by dynamical and previous statistical models in replicating historical interannual SIC observations while making nearly simultaneous predictions evokes a compelling case for a new approach in arctic sea ice minimum extent prediction. Physical–empirical models have been successfully established to predict a variety of meteorological phenomena, in which traditional models often fail. Skillful forecasts of Indian monsoon rainfall (Wang

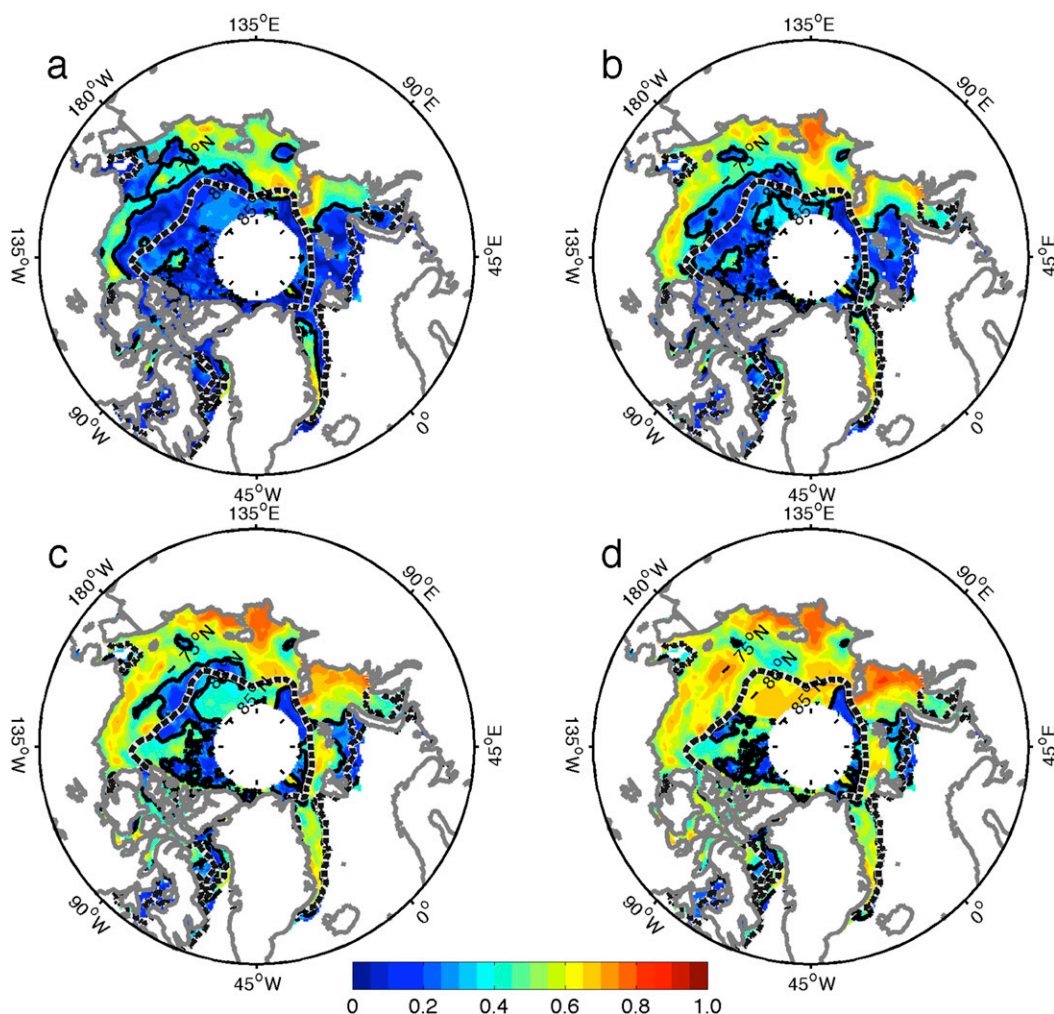


FIG. 16. Correlation coefficients of the (a) AO mode P–E model, (b) combined AO and ISM mode P–E models, and (c) combined AO, ISM, and EASM mode P–E models with the observed interannual SIC from 1979 to 2013 during September–October. (d) Correlation coefficients of the four leading modes only using the predictors with timeframes prior to June with the observed interannual SIC from 1979 to 2013 during September–October. Solid contour represents the 95% significance level while dashed line is the seasonal sea ice zone.

et al. 2015b), summertime upper-tropospheric circulation patterns (Lee et al. 2011), and early summer South China rainfall (Yim et al. 2014b) have been developed using this P–E model approach. The success of P–E models globally and the skill shown for interannual SIC variability prediction in September–October indicate this method could be used for other times of the year, additional arctic variables, and possibly in the Antarctic.

**Acknowledgments.** Bin Wang acknowledges support from NSF Awards AGS-1540783 and NOAA Award NA13OAR4310167. This work is also supported by the Global Research Laboratory (GRL) Program from the National Research Foundation of Korea Grant 2011-0021927 and Atmosphere–Ocean Research Center supported by Nanjing University of Information Science and Technology. We acknowledge the NSIDC, NCEP, ERA, and the Polar Science Center for freely providing data. We also thank the anonymous reviewers for providing constructive comments to improve the quality of the manuscript.

#### REFERENCES

- Adler, R. F., and Coauthors, 2003: The Version-2 Global Precipitation Climatology Project (GPCP) monthly precipitation analysis (1979–present). *J. Hydrometeorol.*, **4**, 1147–1167, doi:10.1175/1525-7541(2003)004<1147:TVGPCP>2.0.CO;2.
- Blanchard-Wrigglesworth, E., and C. M. Bitz, 2014: Characteristics of arctic sea-ice thickness variability in GCMs. *J. Climate*, **27**, 8244–8258, doi:10.1175/JCLI-D-14-00345.1.
- Chevallier, M., and D. Salas-Méla, 2012: The role of sea ice thickness distribution in the arctic sea ice potential predictability: A diagnostic approach with a coupled GCM. *J. Climate*, **25**, 3025–3038, doi:10.1175/JCLI-D-11-00209.1.
- Cohen, J., and Coauthors, 2014: Recent arctic amplification and extreme mid-latitude weather. *Nat. Geosci.*, **7**, 627–637, doi:10.1038/ngeo2234.
- Comiso, J. C., 2000: Bootstrap sea ice concentrations from Nimbus-7 SMMR and DMSP SSM/I-SSMIS, version 2. NASA DAAC at the National Snow and Ice Data Center, accessed 20 October 2013. [Available online at [http://nsidc.org/data/docs/daac/nsidc0079\\_bootstrap\\_seaice.gd.html](http://nsidc.org/data/docs/daac/nsidc0079_bootstrap_seaice.gd.html).]
- Deser, C., 2000: On the teleconnectivity of the “Arctic Oscillation.” *Geophys. Res. Lett.*, **27**, 779–782, doi:10.1029/1999GL010945.
- , and H. Teng, 2008: Evolution of arctic sea ice concentration trends and the role of atmospheric circulation forcing, 1979–2007. *Geophys. Res. Lett.*, **35**, L02504, doi:10.1029/2007GL032023.
- Ding, Q., and B. Wang, 2005: Circumglobal teleconnection in the Northern Hemisphere summer. *J. Climate*, **18**, 3483–3505, doi:10.1175/JCLI3473.1.
- , —, and M. Wallace, 2011: Tropical–extratropical teleconnections in boreal summer: Observed interannual variability. *J. Climate*, **24**, 1878–1896, doi:10.1175/2011JCLI3621.1.
- , J. M. Wallace, D. S. Battisti, E. J. Steig, A. J. Gallant, H. J. Kim, and L. Geng, 2014: Tropical forcing of the recent rapid Arctic warming in northeastern Canada and Greenland. *Nature*, **509**, 209–212, doi:10.1038/nature13260.
- Eicken, H., 2013: Ocean science: Arctic sea ice needs better forecasts. *Nature*, **497**, 431–433, doi:10.1038/497431a.
- Goessling, H. F., S. Tietsche, J. J. Day, E. Hawkins, and T. Jung, 2016: Predictability of the arctic sea ice edge. *Geophys. Res. Lett.*, **43**, 1642–1650, doi:10.1002/2015GL067232.
- Guemas, V., and Coauthors, 2016: A review on arctic sea-ice predictability and prediction on seasonal to decadal time-scales. *Quart. J. Roy. Meteor. Soc.*, **142**, 546–561, doi:10.1002/qj.2401.
- Hawkins, E., S. Tietsche, J. J. Day, N. Melia, K. Haines, and S. Keeley, 2016: Aspects of designing and evaluating seasonal-to-interannual arctic sea-ice prediction systems. *Quart. J. Roy. Meteor. Soc.*, **142**, 672–683, doi:10.1002/qj.2643.
- Hibler, W. D., 1979: A dynamic thermodynamic sea ice model. *J. Phys. Oceanogr.*, **9**, 815–846, doi:10.1175/1520-0485(1979)009<0815:ADTSIM>2.0.CO;2.
- Holland, M. M., C. M. Bitz, B. Tremblay, and D. A. Bailey, 2008: The role of natural versus forced change in future rapid summer arctic ice loss. *Arctic Sea Ice Decline: Observations, Projections, Mechanisms, and Implications*, *Geophys. Monogr.*, Vol. 180, Amer. Geophys. Union, 135–150.
- Honda, M., J. Inoue, and S. Yamane, 2009: Influence of low Arctic sea-ice minima on anomalously cold Eurasian winters. *Geophys. Res. Lett.*, **36**, L08707, doi:10.1029/2008GL037079.
- Hopsch, S., J. Cohen, and K. Dethloff, 2012: Analysis of a link between fall Arctic sea ice concentration and atmospheric patterns in the following winter. *Tellus*, **64A**, 18624, doi:10.3402/tellusa.v64i0.18624.
- Hunke, E. C., and W. H. Lipscomb, 2010: CICE: The Los Alamos Sea Ice Model documentation and software user’s manual, version 4.1. Los Alamos National Laboratory Rep. LA-CC-06-012, 76 pp. [Available online at [http://cdms.colorado.edu/w/images/CICE\\_documentation\\_and\\_software\\_user’s\\_manual.pdf](http://cdms.colorado.edu/w/images/CICE_documentation_and_software_user’s_manual.pdf).]
- Kauker, F., R. Gerdes, M. Karcher, C. Koberle, and J. L. Lieser, 2003: Variability of arctic and North Atlantic sea ice: A combined analysis of model results and observations from 1978 to 2001. *J. Geophys. Res.*, **108**, 3182, doi:10.1029/2002JC001573.
- Kimura, N., and M. Wakatsuchi, 2000: Relationship between sea-ice motion and geostrophic wind in the Northern Hemisphere. *Geophys. Res. Lett.*, **27**, 3735–3738, doi:10.1029/2000GL011495.
- Kwok, R., G. Spreen, and S. Pang, 2013: Arctic sea ice circulation and drift speed: Decadal trends and ocean currents. *J. Geophys. Res.*, **118**, 2408–2425, doi:10.1002/jgrc.20191.
- Lau, K. M., and H. Weng, 2000: Remote forcing of US summertime droughts and floods by the Asian Monsoon? *GEWEX News*, No. 10, International GEWEX Project Office, Silver Spring, MD, 5–6.
- , K. M. Kim, and J. Y. Lee, 2004: Interannual variability, global teleconnection and potential predictability associated with the Asian summer monsoon. *East Asian Monsoon*, C. P. Chang, Ed., World Scientific, 564 pp.
- Lee, J. Y., B. Wang, Q. Ding, K. J. Ha, J. B. Ahn, A. Kumar, B. Stern, and O. Alves, 2011: How predictable is the Northern Hemisphere summer upper-tropospheric circulation? *Climate Dyn.*, **37**, 1189–1203, doi:10.1007/s00382-010-0909-9.
- Lindsay, R. W., J. Zhang, and D. A. Rothrock, 2003: Sea ice deformation rates from measurements and in a model. *Atmos.–Ocean*, **40**, 35–47, doi:10.3137/ao.410103.
- Nitta, T., 1987: Convective activities in the tropical western Pacific and their impact on the Northern Hemisphere summer circulation. *J. Meteor. Soc. Japan*, **65**, 373–390.

- Ogi, M., and K. Yamazaki, 2010: Trends in the summer northern annular mode and arctic sea ice. *SOLA*, **6**, 41–44, doi:[10.2151/sola.2010-011](https://doi.org/10.2151/sola.2010-011).
- Overland, J. E., and C. H. Pease, 1988: Modeling ice dynamics of coastal seas. *J. Geophys. Res.*, **93**, 15 619–15 637, doi:[10.1029/JC093iC12p15619](https://doi.org/10.1029/JC093iC12p15619).
- Plumb, R. A., 1985: On the three-dimensional propagation of stationary waves. *J. Atmos. Sci.*, **42**, 217–229, doi:[10.1175/1520-0469\(1985\)042<0217:OTTDPO>2.0.CO;2](https://doi.org/10.1175/1520-0469(1985)042<0217:OTTDPO>2.0.CO;2).
- Rigor, I. G., and J. M. Wallace, 2004: Variations in the age of arctic sea-ice and summer sea-ice extent. *Geophys. Res. Lett.*, **31**, L09401, doi:[10.1029/2004GL019492](https://doi.org/10.1029/2004GL019492).
- , —, and R. L. Colony, 2002: Response of sea-ice to the Arctic Oscillation. *J. Climate*, **15**, 2648–2663, doi:[10.1175/1520-0442\(2002\)015<2648:ROSITT>2.0.CO;2](https://doi.org/10.1175/1520-0442(2002)015<2648:ROSITT>2.0.CO;2).
- Saji, N. H., B. N. Goswami, P. N. Vinayachandran, and T. Yamagata, 1999: A dipole mode in the tropical Indian Ocean. *Nature*, **401**, 360–363.
- SEARCH, 2015: Sea ice outlook. [Available at <http://www.arcus.org/search/seaiceoutlook/>.]
- Singarayer, J. S., and J. L. Bamber, 2003: EOF analysis of three records of sea-ice concentration spanning the last 30 years. *Geophys. Res. Lett.*, **30**, 1251, doi:[10.1029/2002GL016640](https://doi.org/10.1029/2002GL016640).
- Stroeve, J. C., V. Kattsov, A. Barrett, M. Serreze, T. Pavlova, M. Holland, and W. N. Meier, 2012: Trends in arctic sea ice extent from CMIP5, CMIP3 and observations. *Geophys. Res. Lett.*, **39**, L16502, doi:[10.1029/2012GL052676](https://doi.org/10.1029/2012GL052676).
- , L. C. Hamilton, C. M. Bitz, and E. B. Wrighlesworth, 2014: Predicting September sea ice: Ensemble skill of the SEARCH sea ice outlook 2008–2013. *Geophys. Res. Lett.*, **41**, 2411–2418, doi:[10.1002/2014GL059388](https://doi.org/10.1002/2014GL059388).
- Tang, Q., X. Zhang, X. Yang, and J. A. Francis, 2013: Cold winter extremes in northern continents linked to arctic sea ice loss. *Environ. Res. Lett.*, **8**, 014036, doi:[10.1088/1748-9326/8/1/014036](https://doi.org/10.1088/1748-9326/8/1/014036).
- Thorndike, A. S., and R. Colony, 1982: Sea ice motion in response to geostrophic winds. *J. Geophys. Res.*, **87**, 5845–5852, doi:[10.1029/JC087iC08p05845](https://doi.org/10.1029/JC087iC08p05845).
- , D. A. Rothrock, G. A. Maykut, and R. Colony, 1975: The thickness distribution of sea ice. *J. Geophys. Res.*, **80**, 4501–4513, doi:[10.1029/JC080i033p04501](https://doi.org/10.1029/JC080i033p04501).
- Vihma, T., 2014: Effects of arctic sea ice decline on weather and climate: A review. *Surv. Geophys.*, **35**, 1175–1214, doi:[10.1007/s10712-014-9284-0](https://doi.org/10.1007/s10712-014-9284-0).
- , P. Tisler, and P. Uotila, 2012: Atmospheric forcing on the drift of arctic sea ice in 1989–2009. *Geophys. Res. Lett.*, **39**, L02501, doi:[10.1029/2011GL050118](https://doi.org/10.1029/2011GL050118).
- Walsh, J. E., 1980: Empirical orthogonal functions and the statistical predictability of sea ice extent. *Sea Ice Processes and Models*, R. S. Pritchard, Ed., University of Washington Press, 373–384.
- Wang, B., and X. Xie, 1996: Low-frequency equatorial waves in vertically sheared flows. Part I: Stable waves. *J. Atmos. Sci.*, **53**, 449–467, doi:[10.1175/1520-0469\(1996\)053<0449:LFEWIV>2.0.CO;2](https://doi.org/10.1175/1520-0469(1996)053<0449:LFEWIV>2.0.CO;2).
- , R. Wu, and X. Fu, 2000: Pacific–East Asian teleconnection: How does ENSO affect East Asian climate? *J. Climate*, **13**, 1517–1536, doi:[10.1175/1520-0442\(2000\)013<1517:PEATHD>2.0.CO;2](https://doi.org/10.1175/1520-0442(2000)013<1517:PEATHD>2.0.CO;2).
- , —, and K. M. Lau, 2001: Interannual variability of the Asian summer monsoon: Contrasts between the Indian and the western North Pacific–East Asian monsoon. *J. Climate*, **14**, 4073–4090, doi:[10.1175/1520-0442\(2001\)014<4073:IVOTAS>2.0.CO;2](https://doi.org/10.1175/1520-0442(2001)014<4073:IVOTAS>2.0.CO;2).
- , —, and T. Li, 2003: Atmosphere–warm ocean interaction and its impact on Asian–Australian monsoon variation. *J. Climate*, **16**, 1195–1211, doi:[10.1175/1520-0442\(2003\)16<1195:AOIAII>2.0.CO;2](https://doi.org/10.1175/1520-0442(2003)16<1195:AOIAII>2.0.CO;2).
- , I. S. Kang, and J. Y. Lee, 2004: Ensemble simulations of Asian–Australian monsoon variability by 11 AGCMs. *J. Climate*, **17**, 803–818, doi:[10.1175/1520-0442\(2004\)017<0803:ESOAMV>2.0.CO;2](https://doi.org/10.1175/1520-0442(2004)017<0803:ESOAMV>2.0.CO;2).
- , J. Y. Lee, and B. Xiang, 2015a: Asian summer monsoon rainfall predictability: A predictable mode analysis. *Climate Dyn.*, **44**, 61–74, doi:[10.1007/s00382-014-2218-1](https://doi.org/10.1007/s00382-014-2218-1).
- , B. Xiang, J. Li, P. J. Webster, M. N. Rajeevan, J. Liu, and K.-J. Ha, 2015b: Rethinking Indian monsoon rainfall prediction in the context of recent global warming. *Nat. Commun.*, **6**, 7154, doi:[10.1038/ncomms8154](https://doi.org/10.1038/ncomms8154).
- Watanabe, E., and H. Hasumi, 2005: Arctic sea ice response to wind stress variations. *J. Geophys. Res.*, **110**, C11007, doi:[10.1029/2004JC002678](https://doi.org/10.1029/2004JC002678).
- Webster, P. J., A. Moore, J. Loschnigg, and M. Leban, 1999: Coupled ocean–atmosphere dynamics in the Indian Ocean during 1997–98. *Nature*, **401**, 356–360, doi:[10.1038/43848](https://doi.org/10.1038/43848).
- Wettstein, J. J., and C. Deser, 2014: Internal variability in projections of twenty-first-century arctic sea ice loss: Role of the large-scale atmospheric circulation. *J. Climate*, **27**, 527–550, doi:[10.1175/JCLI-D-12-00839.1](https://doi.org/10.1175/JCLI-D-12-00839.1).
- Xiang, B., W. Yu, T. Li, and B. Wang, 2011: The critical role of the boreal summer mean state in the development of the IOD. *Geophys. Res. Lett.*, **38**, L02710, doi:[10.1029/2010GL045851](https://doi.org/10.1029/2010GL045851).
- Xie, P., and P. A. Arkin, 1997: Global precipitation: A 17-year monthly analysis based on gauge observations, satellite estimates, and numerical model outputs. *Bull. Amer. Meteor. Soc.*, **78**, 2539–2558, doi:[10.1175/1520-0477\(1997\)078<2539:GPAYMA>2.0.CO;2](https://doi.org/10.1175/1520-0477(1997)078<2539:GPAYMA>2.0.CO;2).
- Yim, S. Y., B. Wang, J. Liu, and Z. Wu, 2014a: A comparison of regional monsoon variability using monsoon indices. *Climate Dyn.*, **43**, 1423–1437, doi:[10.1007/s00382-013-1956-9](https://doi.org/10.1007/s00382-013-1956-9).
- , —, and W. Xing, 2014b: Prediction of early summer rainfall over South China by a physical-empirical model. *Climate Dyn.*, **43**, 1883–1891, doi:[10.1007/s00382-013-2014-3](https://doi.org/10.1007/s00382-013-2014-3).
- Zhang, J., and D. A. Rothrock, 2003: Modeling global sea ice with a thickness and enthalpy distribution model in generalized curvilinear coordinates. *Mon. Wea. Rev.*, **131**, 681–697, doi:[10.1175/1520-0493\(2003\)131<0845:MGSIIWA>2.0.CO;2](https://doi.org/10.1175/1520-0493(2003)131<0845:MGSIIWA>2.0.CO;2).
- Zhao, Y., and A. K. Liu, 2007: Arctic sea-ice motion and its relation to pressure field. *J. Oceanogr.*, **63**, 505–515, doi:[10.1007/s10872-007-0045-2](https://doi.org/10.1007/s10872-007-0045-2).
- Zhou, X., 2014: Rapid change of the arctic sea ice and response of dominant modes of atmosphere. M.S. thesis, College of Oceanic and Atmospheric Sciences, Ocean University of China, 80 pp.